THE GEOLOGICAL SOCIETY OF AMERICA®

Uplift and exhumation of the Russell Fiord and Boundary blocks along the northern Fairweather transform fault, Alaska

Anna Schartman[1], Eva Enkelmann[2,*], John I. Garver[3], and Cameron M. Davidson[4]
[1]DEPARTMENT OF GEOLOGY, UNIVERSITY OF CINCINNATI, 500 GEOLOGY PHYSICS BUILDING, CINCINNATI, OHIO 45221-0013, USA
[2]DEPARTMENT OF GEOSCIENCE, UNIVERSITY OF CALGARY, 2500 UNIVERSITY DRIVE N.W., CALGARY, ALBERTA, T2N 1N4, CANADA
[3]DEPARTMENT OF GEOLOGY, UNION COLLEGE, 807 UNION STREET, SCHENECTADY, NEW YORK 12308-2311, USA
[4]DEPARTMENT OF GEOLOGY, CARLETON COLLEGE, ONE NORTH COLLEGE STREET, NORTHFIELD, MINNESOTA 55057, USA

ABSTRACT

Cooling ages of tectonic blocks between the Yakutat microplate and the Fairweather transform boundary fault reveal exhumation due to strike-slip faulting and subsequent collision into this tectonic corner. The Yakutat and Boundary faults are splay faults that define tectonic panels with bounding faults that have evidence of both reverse and strike-slip motion, and they are parallel to the northern end of the Fairweather fault. Uplift and exhumation simultaneous with strike-slip motion have been significant since the late Miocene. The blocks are part of an actively deforming tectonic corner, as indicated by the ~14–1.5 m of coseismic uplift from the M 8.1 Yakutat Bay earthquake of 1899 and 4 m of strike-slip motion in the M 7.9 Lituya Bay earthquake in 1958 along the Fairweather fault. New apatite (U-Th-Sm)/He (AHe) and zircon (U-Th)/He (ZHe) data reveal that the Boundary block and the Russell Fiord block have different cooling histories since the Miocene, and thus the Boundary fault that separates them is an important tectonic boundary. Upper Cretaceous to Paleocene flysch of the Russell Fiord block experienced a thermal event at 50 Ma, then a relatively long period of burial until the late Miocene when initial exhumation resulted in ZHe ages between 7 and 3 Ma, and then very rapid exhumation in the last 1–1.5 m.y. Exhumation of the Russell Fiord block was accommodated by reverse faulting along the Yakutat fault and the newly proposed Calahonda fault, which is parallel to the Yakutat fault. The Eocene schist of Nunatak Fiord and 54–53 Ma Mount Stamy and Mount Draper granites in the Boundary block have AHe and ZHe cooling ages that indicate distinct and very rapid cooling between ca. 5 Ma and ca. 2 Ma. Rocks of the Chugach Metamorphic Complex to the northeast of the Fairweather fault and in the fault zone were brought up from 10–12 km at extremely high rates (>5 km/m.y.) since ca. 3 Ma, which implies a significant component of dip-slip motion along the Fairweather fault. The adjacent rocks of the Boundary block were exhumed with similar rates and from similar depths during the early Pliocene, when they may have been located 220–250 km farther south near Baranof Island. The profound and significant exhumation of the three tectonic blocks in the last 5 m.y. has probably been driven by uplift and erosional exhumation due to contraction as rocks collide into this tectonic corner. The documented spatial and temporal pattern of exhumation is in agreement with the southward shift of focused exhumation at the St. Elias syntaxial corner and the southeast propagation of the fold-and thrust belt.

LITHOSPHERE GSA Data Repository Item 2019033 https://doi.org/10.1130/L1011.1

INTRODUCTION

The structural disposition of tectonic blocks at continental plate boundaries can be complex in plate corners where the strikes of structures change and rocks transition to a different tectonic regime. Such a structurally complex corner region is exposed in coastal central to southeast Alaska at the active Yakutat–North American plate boundary, where rocks get transferred from a strike-slip margin to collisional margin. In this region, the NNW-trending dextral Fairweather transform boundary transitions to the NE-trending fold-and-thrust belt system of the St. Elias Mountains (Fig. 1). Several splay faults with reverse dip-slip motion run parallel to the northern end of the Fairweather fault and result in NE-SW shortening within the Yakutat microplate before the entire microplate is thrust underneath the North American plate, where NW-SE shortening occurs across the orogenic belt.

Here, we present new thermochronologic data from the Yakutat Bay area that reveal the timing, rates, and amounts of rock exhumation accommodated by the reverse and thrust faults that deform the Yakutat microplate as it is transported along the Fairweather fault into the collisional corner setting of the St. Elias Mountains. We integrated our new data with existing bedrock and detrital data sets to reveal the structural evolution of this accreted microplate. The high spatial resolution of the integrated data set reveals a new splay fault that was previously undetected, and it appears to play an important role in partitioning strain along this part of the margin.

GEOLOGIC BACKGROUND

The Yakutat microplate in the northern Gulf of Alaska is a 15–30-km-thick wedge-shaped composite terrane of oceanic plateau rocks and

Eva Enkelmann http://orcid.org/0000-0002-1988-0760
*Corresponding author

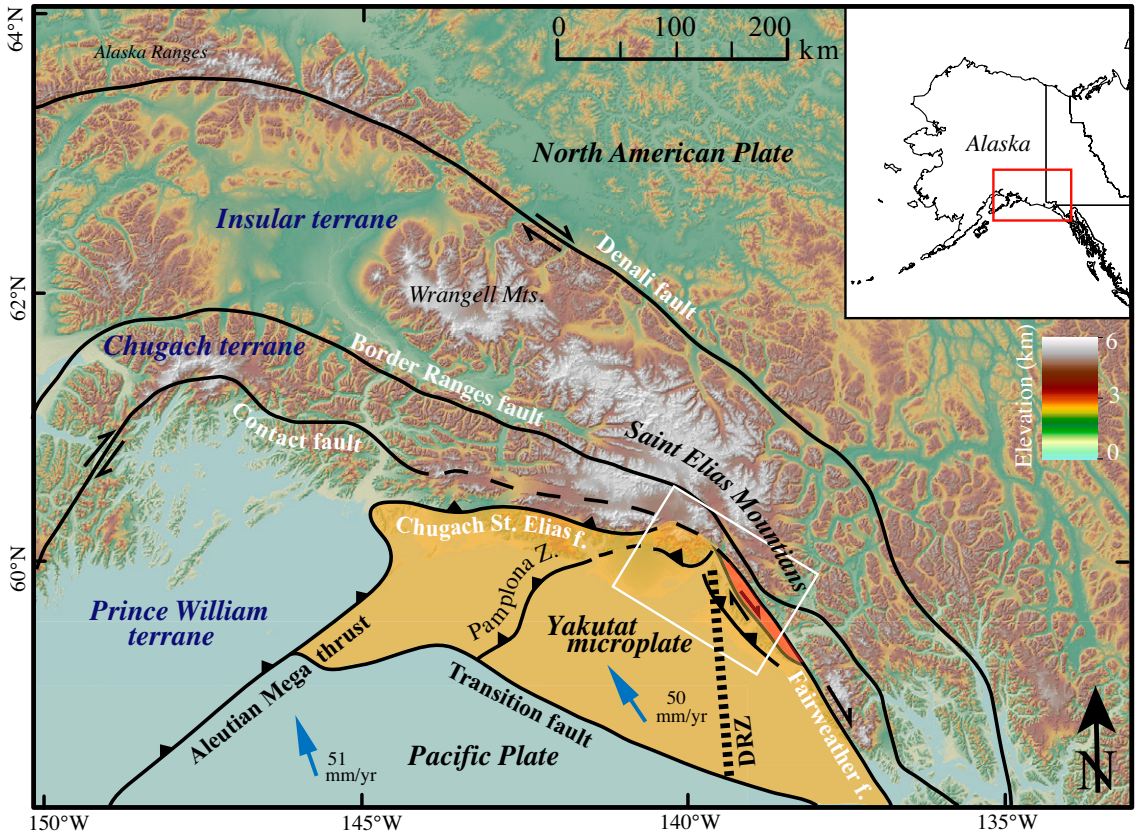

Figure 1. Topographic map of coastal south-central and southeast Alaska. Block outlined in yellow shows the surface extent of the Yakutat microplate. The tectonic sliver shown in red is the fault-bounded Boundary block, which is allied with the Chugach–Prince William terrane. White box outlines the study area at the northern end of the Fairweather plate boundary and the map area shown in Figure 2. DRZ—Dangerous River zone. Plate motion is from Elliott et al. (2010).

structurally overlying flysch and mélange that is subducting underneath the North American plate (Plafker et al., 1994; Christeson et al., 2010). The microplate is currently moving at a rate of 50 mm/yr to the NNW, and it is colliding obliquely with southeastern Alaska (Sauber et al., 1997; Fletcher and Freymueller, 1999). The Yakutat–North American plate boundary is defined to the east by the Fairweather transform, which transitions to the Chugach St. Elias thrust in the north, and the Aleutian megathrust in the west (Fig. 1). To the south, the right-lateral Transition fault marks the boundary between the Yakutat microplate and the Pacific plate (Fig. 1; Gulick et al., 2007; Christeson et al., 2010). Plate reorganization at around 50 Ma resulted in the development of the dextral Queen Charlotte–Fairweather fault system, which carried the Yakutat microplate northward to its present location (Bruns, 1983; Plafker et al., 1994; Bruhn et al., 2004; Pavlis et al., 2004; Perry et al., 2009). The subduction of the thick microplate under the North American continent resulted in flat-slab subduction in southern Alaska (Abers, 2008; Haeussler, 2008; Finzel et al., 2011), and building of the St. Elias Mountains in coastal southeast Alaska (Bruhn et al., 2004; Berger et al., 2008a; Enkelmann et al., 2008, 2010, 2017; Falkowski et al., 2016).

Inboard of the active plate boundary, the North American plate consists of several terranes that have been accreted to the continental margin since the Mesozoic (Fig. 1; Plafker et al., 1994; Garver and Davidson, 2015; Davidson and Garver, 2017). Immediately inboard of the active plate boundary, there is the Chugach–Prince William terrane, dominated by upper Cretaceous to Eocene flysch, but it also includes older mélange units (Garver and Davidson, 2015; Davidson and Garver, 2017). The Chugach–Prince William terrane is separated from the inboard Insular terrane (Wrangellia and Alexander terranes) by the Border Ranges fault. The Chugach–Prince William terrane was intruded by the time-transgressive Sanak-Baranof plutonic belt, which is younger eastward, from 61 to 48 Ma (Hudson et al., 1979; Farris and Paterson, 2009; Haeussler et al., 1995, 2003; Davidson and Garver, 2017). Near-trench magmatism of the Sanak-Baranof plutonic belt caused high-temperature and low-pressure metamorphism of the Chugach Metamorphic Complex (CMC), which is exposed in the core of the St. Elias Mountains, and also of the Baranof Schist to the south on Baranof Island in southeast Alaska. The CMC is composed of a zone of schist and migmatitic gneisses, and a zone of metabasalts and metasedimentary rock of greenschist to amphibolite facies (Gasser et al., 2011). Near the northern terminus of the Fairweather fault, the CMC consists of a northeastern unit of gneisses and schists and a southwestern unit of fine-grained amphibolites (Gasser et al., 2011). On the east side of the Border Ranges fault, the Insular terrane is a composite terrane characterized by a late Paleozoic–early Mesozoic oceanic plateau and island-arc assemblages accreted to North America by the Late Cretaceous (Jones et al., 1977; Gardner et al., 1988; Plafker et al., 1989, 1994; Trop et al., 2002). In this part of Alaska and southwest Yukon, the Insular terrane has a cover sequence of Oligocene to Holocene volcanic rocks, and it is intruded by plutonic rocks of the Wrangell Mountains, which have been linked to the subduction of the Yakutat microplate (Richter et al., 1990).

As traditionally defined, the Yakutat microplate comprises two basement units: (1) an Eocene oceanic basaltic plateau, which is structurally separated by the Dangerous River fault from (2) the structurally

overlying flysch and mélange of the Cretaceous–Paleocene Yakutat Group (Worthington et al., 2012; Garver and Davidson, 2017). These basement units are overlain by up to 12-km-thick deformed Cenozoic sedimentary cover rocks. The cover strata comprise the middle Eocene to early Miocene Kultieth, Stillwater, and Poul Creek Formations (Plafker, 1987; Trop and Ridgway, 2007; Perry et al., 2009), and the glacial-derived Yakataga Formation, which records latest Miocene to Pleistocene erosion of the adjacent orogenic highlands and deposition of recycled material that is partly derived from the Chugach–Prince William terrane (Lagoe et al., 1993; Plafker et al., 1994; Zellers, 1995; Perry et al., 2009). The sedimentary cover strata have been investigated offshore and are well exposed in a fold-and-thrust belt west of Malaspina Glacier. East of the Malaspina Glacier, the basement units of the Yakutat Group are mainly exposed. The Yakutat Group has been interpreted as the remnant of an accretionary prism, and it is composed of highly deformed flysch and mélange sequences that have been subjected to low-grade metamorphism (Hudson et al., 1977; Dusel-Bacon et al., 1993). Although it was suggested that the Yakutat Group constituted the southernmost block of the Chugach–Prince William terrane prior to its juxtaposition in southeastern Alaska (Plafker et al., 1994; Haeussler et al., 2003; Garver and Davidson, 2015), more recent studies have shown that these units have different ages and have distinctly different provenances and thus cannot be correlated (Davidson and Garver, 2017; Garver and Davidson, 2017; Olson et al., 2017).

Yakutat Bay Area

The study area is located at the colliding corner of the Yakutat microplate where the Fairweather transform boundary transitions into convergence, manifested by the fold-and-thrust belt of the collision zone in the St. Elias Mountains. This region is characterized by three crustal blocks separated by north-northwest–striking faults with oblique slip that are parallel to the Fairweather fault (Fig. 2). From northeast to southwest, these are the dextral Fairweather fault, the Boundary fault, and the Yakutat fault (Fig. 2). The Yakutat fault, the most outboard, is inferred to dip between 30° and 60° to the northeast and allows the Russell Fiord block to thrust upwards toward the southwest over the foreland (Plafker and Thatcher, 2008; Bruhn et al., 2012; Chapman et al., 2012). (Note: In southern Alaska, both Fjord and Fiord are commonly used. Here, we defer to U.S. Geological Survey [USGS] usage and use Fiord throughout this paper.) A steeper dip with a greater strike-slip component is proposed for the Boundary fault (Sisson et al., 2003; Elliott et al., 2010; Enkelmann et al., 2015a), but the exact geometry of both faults is unknown. The current motion along these faults has been studied by global positioning system (GPS) measurements, and the derived block models estimate 42.9 ± 0.9 mm/yr of pure strike-slip motion along the Fairweather fault, while the Yakutat fault accommodates convergent motion of 4.6 ± 0.9 mm/yr (Elliott et al., 2010). To fit the measurements, the GPS model requires the existence of at least one additional block (Boundary block) and predicts an average of 3.6 ± 1.4 mm/yr of right-lateral strike-slip motion with a small dip-slip component (Elliott et al., 2010). These three faults juxtapose differing lithologies and metamorphic grades against each other, suggesting different provenance and deformation histories for each crustal block. At a regional scale, the Boundary and Yakutat faults undoubtedly project to the Chaix Hills and the Esker Creek faults located west of Disenchantment Bay. The strike of these faults changes from NNW to WNW across Disenchantment Bay (Fig. 2). Thus, we are interested in understanding the tectonic evolution of the three main crustal blocks and their kinematic relationship to the structures that occur in this tectonic corner.

The Russell Fiord block is located between the Yakutat and Boundary faults and includes rocks of the Yakutat Group flysch and mélange facies that we have studied extensively (Fig. 2). The mélange is a sedimentary mélange dominated by phacoids, knockers, and tectonic slices of coarse sandstone, but it also includes blocks of metaplutonic rocks, greenstone, limestone, and chert (Garver and Davidson, 2015; Dolcimascolo et al., 2017; Garver and Davidson, 2017; Sophis et al., 2017). The plutonic clasts and knockers in the mélange unit have Jurassic zircon U-Pb ages between 175 and 167 Ma (Dolcimascolo et al., 2017). Many of the sandstones are arkosic, and they locally include sections of pebble conglomerate that are dominated by sedimentary lithologies. The flysch facies of the Yakutat Group is composed of turbidites from slope, fan, and basin plain depositional settings, and the unit is composed of interlayered beds of argillaceous mudstone and sandstone of various thicknesses. The provenance of the sandstone of the flysch is identical to the arkose of the mélange, and detrital zircon dating constrains the ages of these clastic units to be mainly Maastrichtian to Paleocene (Sophis et al., 2017).

The Boundary block is a thin (5–10 km) tectonic sliver of schistose meta-turbidites located between the Boundary and the Fairweather faults (Fig. 2). These rocks were originally mapped as a separate and distinct unit from the adjacent Yakutat rocks (Tarr and Butler, 1909), and they were later grouped with the Yakutat Group (see Plafker et al., 1994), but now they have been shown to be a distinct unit correlative to the Chugach–Prince William terrane, and not the Yakutat Group (Garver and Davidson, 2017; Olson et al., 2017). The schist is composed of higher-grade metamorphic rocks mapped as the schist of Nunatak Fiord (abbreviated SNF and depicted in Fig. 2), an informal term coined during regional mapping (Richter et al., 2006). The schists of the Boundary block have been intruded by tonalite-granodiorite, granite, diorite, and gabbro. The largest intrusion is the 54–53 Ma Mount Draper Pluton, which is part of the Sanak-Baranof magmatic belt (Sisson et al., 2003; Arnston et al., 2017). In the area of Nunatak Fiord, the Fairweather fault zone is characterized by highly deformed rocks of amphibolite and metasediments of the CMC that are related to the Chugach–Prince William terrane. The large valley of the fault zone and the area to the northeast are composed of well-foliated and folded garnet-bearing metavolcanic amphibolites, schists, and gneisses of the Chugach metamorphic complex, containing felsic dikes and veins. Farther away from the fault zone, the amphibolite is layered with metagraywacke (Sisson et al., 2003).

METHODS

We collected 20 rock samples from the Russell Fiord and Boundary blocks, as well as from within and east of the Fairweather fault zone. All samples were collected at sea level along the shores of Yakutat Bay, Disenchantment Bay, and Nunatak and Russell Fiords (Fig. 2). This sampling strategy was dictated by boat access, and it allowed us to create a uniform reference that records the differential exhumation that has been accommodated along the three fault systems. From the Russell Fiord block, we collected medium- to coarse-grained sandstone from the mélange and flysch facies of the Yakutat Group, including a tonalite sample from a large tectonic block in the mélange (Table 1). We collected metasandstone from the schist of Nunatak Fiord and granite from the Boundary block, and fine-grained amphibolite from the Fairweather fault zone. We separated zircon and apatite using standard methods of crushing, sieving, and magnetic and heavy liquid separation, and all 20 rock samples yielded both apatite and zircon grains.

Individual apatite and zircon grains were inspected and analyzed using a Zeiss stereomicroscope to select euhedral inclusion-free grains with width >80 μm. For each apatite sample, we aimed to analyze five single-grain or multigrain aliquots. The multigrain aliquots were necessary because of the low helium yield in some samples. Three single zircon grains were analyzed per sample. After inspection and measurement of

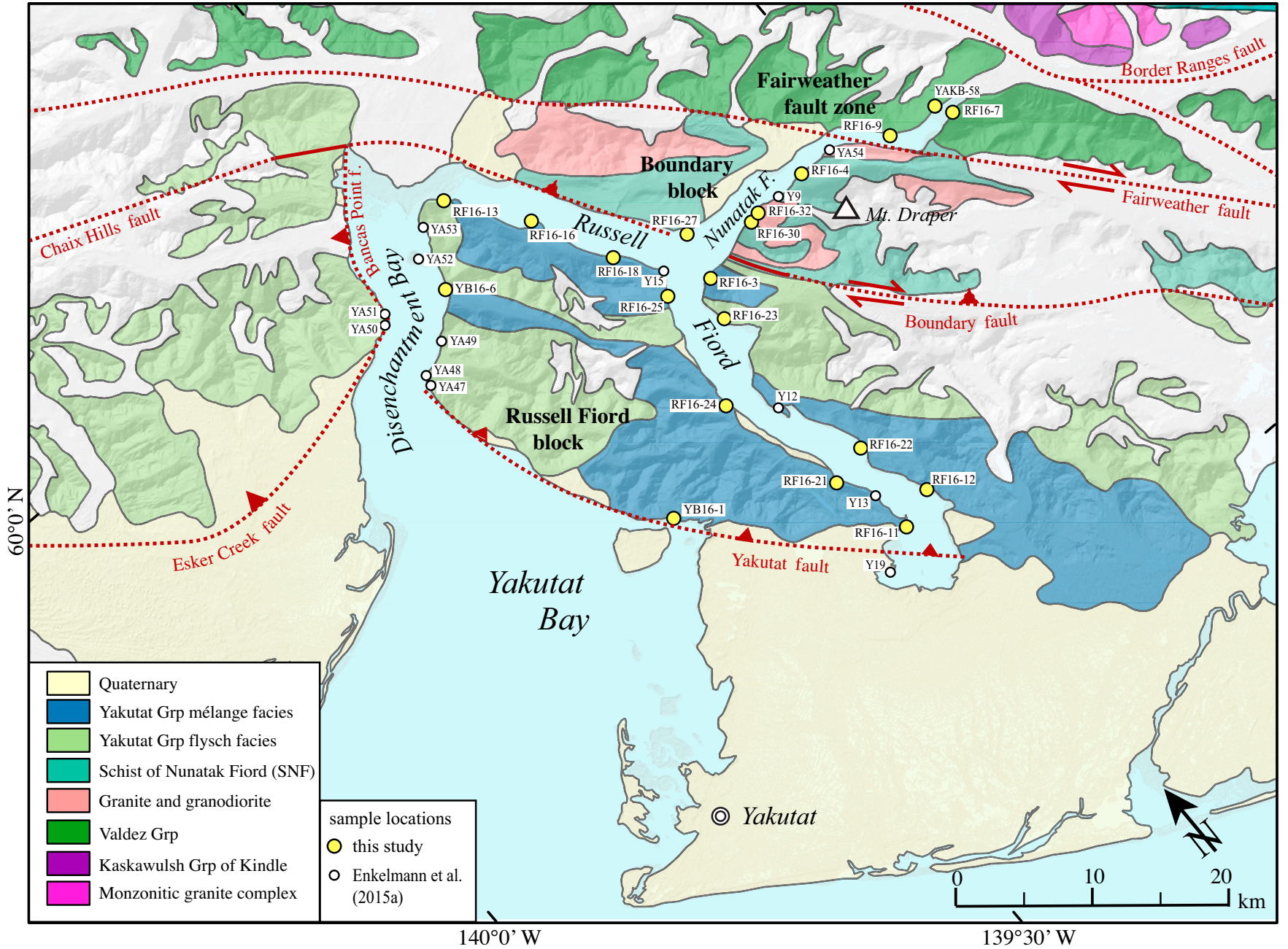

Figure 2. Bedrock geologic map of the Yakutat Bay, Russell Fiord, and Nunatak Fiord region depicting new sample locations (large circles) and published sample locations (small circles). Base map is modified from Wilson et al. (2015) and Cui et al. (2017). F.—Fiord; f.—fault; Grp—Group.

TABLE 1. SAMPLE LOCATION AND DESCRIPTION

Sample ID	Latitude (°N)	Longitude (°W)	Geologic unit	Rock type
Yakutat block				
YB16-01	59.72032	139.50494	Yakutat Group mélange facies	Sandstone
YB16-06	59.94009	139.53526	Yakutat Group mélange facies	Sandstone
RF16-03	59.82948	139.27042	Yakutat Group flysch facies	Sandstone
RF16-11	59.61415	139.28807	Yakutat Group mélange facies	Sandstone
RF16-12	59.62328	139.24001	Yakutat Group mélange facies	Sandstone clast
RF16-13	59.98639	139.46452	Yakutat Group flysch facies	Sandstone
RF16-16	59.93722	139.39713	Yakutat Group tonalite mass	Biotite-hornblende-quartz diorite
RF16-18	59.88166	139.34904	Yakutat Group mélange facies	Sandstone
RF16-21	59.66721	139.31909	Yakutat Group mélange facies	Sandstone
RF16-22	59.67433	139.26836	Yakutat Group mélange facies	Sandstone
RF16-23	59.80011	139.29527	Yakutat Group flysch facies	Sandstone
RF16-24	59.75628	139.36179	Yakutat Group mélange facies	Sandstone
RF16-25	59.83974	139.32799	Yakutat Group mélange facies	Sandstone
Boundary block				
RF16-04	59.84210	139.09860	Schist of Nunatak Fjord	Sandstone
RF16-27	59.86171	139.25586	Schist of Nunatak Fjord	Sandstone
RF16-30	59.84126	139.18379	Mount Draper Pluton	Two-mica granite
RF16-32	59.84215	139.17502	Mount Draper Pluton	Two-mica granite
Fairweather fault zone				
RF16-07	59.80631	138.90431	Valdez Group schistose metaflysch	Amphibolite
RF16-09	59.82297	138.98213	Valdez Group schistose metaflysch	Garnet amphibolite

the dimensions, the grains were packed into niobium tubes and sent for (U-Th-Sm)/He analysis at the Thermochronology Research and Instrumentation Laboratory at the University of Colorado at Boulder.

RESULTS

We present new apatite (U-Th-Sm)/He (AHe) data from 18 samples (Table 2), and new zircon (U-Th)/He (ZHe) data from 11 samples (Table 3). The AHe single-grain ages, ranging from 0.18 ± 0.24 Ma to 7.26 ± 1.10 Ma, reproduced the sample age well (Table 2). Mean ages were calculated for each sample, ranging from 0.57 ± 0.10 Ma to 2.54 ± 0.40 Ma (Table 2; Fig. 3). From the 88 AHe dates, 12 aliquot dates were identified as outliers and were not considered for calculating the mean age (Table 2). There are a variety of reasons for such outlier data (Fitzgerald et al., 2006), and we consider inclusions and zonation of U and Th as the most likely sources in our data set. Because most of our apatite grains are from sediment and metasedimentary rocks, the crystal surfaces are commonly rough, and thus the lower transparency of these rough surfaces obstructs inspection of grain interiors. Another reason for intersample age dispersions is the variations in grain size and radiation damage, which are particularly pronounced in slowly cooled samples (Farley, 2002). Here, we plotted the single-grain AHe ages against the effective uranium concentration (eU), which is used as an indicator for radiation damage (Flowers et al., 2007), and we plotted the AHe ages against the spherical radius (Rs) to explore such relationships (GSA Data Repository Fig. S1[1]). There are no obvious correlations that would explain the outlier data, which is in agreement with the generally young AHe data that indicate rapid cooling through the helium partial retention zone (PRZ) for apatite (Farley, 2002). In general, the mean AHe ages from the Russell Fiord block range from 0.6 ± 0.1 Ma to 1.5 ± 0.2 Ma, while samples from the Boundary block are older and range between 1.47 ± 0.01 Ma and 2.5 ± 0.4 Ma (Table 2). The two samples from the Fairweather fault zone yield identical mean AHe ages of 0.7 ± 0.4 Ma and 0.8 ± 0.1 Ma (Fig. 3).

We report 34 new ZHe ages from 11 samples (Table 3). Samples from the Russell Fiord block yield single-grain ZHe ages ranging between 2.81 ± 0.20 Ma and 57.5 ± 4.20 Ma, while ZHe ages from the Boundary block are generally younger and range between 4.89 ± 0.40 Ma and 22.7 ± 1.60 Ma (Table 3). One sample was dated from the Fairweather fault zone, yielding a mean age of 0.8 ± 0.2 Ma. For both the Russell Fiord and Boundary blocks, the ZHe ages are younger closer to the trace of the Yakutat and Boundary faults, respectively (Fig. 3). In general all samples reveal a wide spread between single-grain ZHe ages, which is indicative of rocks that experienced a prolonged residence within the temperature zone of the PRZ (e.g., Farley, 2002; Fitzgerald et al., 2006; Guenthner et al., 2013). Such a thermal history causes significant variations in helium retention that depends on the grain size and radiation damage (Guenthner et al., 2014). In general, the helium ages are expected to increase with increasing grain size (Farley, 2002), and increasing accumulation of radiation damage, which is inferred to impede diffusion (Guenthner et al., 2013). Recent studies have shown that this positive correlation between ZHe age and eU does not occur past a certain threshold of damage, and at higher damage, the opposite relationship occurs. Diffusion of helium is facilitated by damage, and ZHe ages correlate negatively with eU (Guenthner et al., 2013). When plotting our ZHe ages against Rs and eU, we see this general trend for some samples with ZHe data older than ca. 18 Ma, but the younger ZHe data do not show correlation with Rs or eU (Data Repository Fig. S2). Within the older data, grains with eU higher than 500–700 ppm are negatively correlated with age. In contrast, no correlation is observed for samples that cooled more recently (ZHe ages <18 Ma) and yield less age dispersion, which are generally the samples located close to the Yakutat fault (YB16–01, YB16–06) or samples from the Boundary block (RF16–04, RF16–27).

THERMAL HISTORY MODELING

To investigate the thermal history of our samples, we used inverse modeling of the cooling ages to find possible time-temperature paths (*t-T*

[1]GSA Data Repository Item 2019033, AHe and ZHe data plotted against uranium concentration and grain radii, thermal history model parameters, and results of individual samples, is available at http://www.geosociety.org/datarepository/2019, or on request from editing@geosociety.org.

TABLE 2. APATITE (U-Th-Sm)/He DATA

Sample ID	*N*	^{4}He (nmol/g)	U (ppm)	Th (ppm)	Sm (ppm)	eU (ppm)	rs (μm)	Raw age (Ma)	Ft	Corrected age (Ma)
Yakutat block										
YB16-01_1	1	1.009	348	101	64.7	371	36.5	0.5 ± 0.01	0.631	0.80 ± 0.05
YB16-01_3	1	1.230	71.9	4.60	58.7	72.9	47.9	3.11 ± 0.08	0.715	*4.34 ± 0.32*
YB16-01_4	1	0.144	29.1	28.8	64.9	35.8	42.4	0.74 ± 0.07	0.669	1.09 ± 0.14
YB16-01_5	1	0.165	54.0	89.5	16.4	75.0	45.4	0.41 ± 0.02	0.688	0.59 ± 0.05
YB16-01_6	3	0.365	90.2	149	59.2	125	43.4	0.54 ± 0.02	0.674	0.80 ± 0.06
YB16-01_7	1	1.074	135	118	103	162	45.8	1.22 ± 0.03	0.696	*1.75 ± 0.12*
									Mean age:	**0.82 ± 0.21**
YB16-06_1	1	0.016	5.59	7.38	5.26	7.30	38.6	0.39 ± 0.21	0.640	0.61 ± 0.33
YB16-06_2	1	0.261	37.7	96.4	49.6	60.4	42.1	0.79 ± 0.03	0.659	1.20 ± 0.10
YB16-06_3	1	0.500	107	53.9	71.9	120	39.0	0.77 ± 0.03	0.650	1.18 ± 0.09
YB16-06_4	1	0.108	24.6	19.5	42.1	29.2	37.8	0.68 ± 0.09	0.636	1.06 ± 0.16
YB16-06_5	1	0.108	21.1	18.9	14.2	25.6	40.9	0.78 ± 0.07	0.662	1.18 ± 0.14
									Mean age:	**1.16 ± 0.06**
RF16-03_1	1	0.104	10.0	31.6	29.0	17.5	51.6	1.09 ± 0.04	0.713	1.52 ± 0.12
RF16-03_2	1	0.260	38.3	110	37.6	64.2	47.6	0.74 ± 0.03	0.692	1.07 ± 0.09
RF16-03_3	1	0.110	21.2	47.6	11.0	32.4	51.1	0.63 ± 0.03	0.718	0.87 ± 0.07
RF16-03_4	1	0.171	25.1	73.4	34.7	42.4	46.9	0.74 ± 0.03	0.689	1.07 ± 0.09
RF16-03_5	1	0.069	11.4	35.0	10.4	19.6	41.9	0.65 ± 0.10	0.657	0.99 ± 0.16
									Mean age:	**1.10 ± 0.25**
RF16-11_1	2	0.135	46.5	52.6	85.6	58.8	55.0	0.42 ± 0.05	0.742	0.56 ± 0.08
RF16-11_2	2	0.134	24.5	57.7	71.8	38.0	57.0	0.64 ± 0.04	0.746	0.86 ± 0.08
RF16-11_3	2	0.201	43.7	121	60.6	72.2	48.8	0.51 ± 0.03	0.703	0.73 ± 0.06
RF16-11_4	1	0.038	12.1	12.6	25.6	15.1	61.1	0.46 ± 0.05	0.770	0.60 ± 0.07
									Mean age:	**0.69 ± 0.14**
RF16-12_1	1	0.058	4.18	17.9	12.2	8.40	74.2	1.27 ± 0.05	0.798	*1.58 ± 0.13*
RF16-12_2	1	0.062	4.40	9.30	8.51	6.60	67.5	1.73 ± 0.09	0.783	*2.20 ± 0.19*
RF16-12_3	1	0.109	15.2	56.1	15.4	28.4	67.1	0.71 ± 0.03	0.778	0.91 ± 0.07
RF16-12_4	1	0.033	1.76	24.8	15.6	7.60	71.0	0.79 ± 0.06	0.781	1.00 ± 0.10
RF16-12_5	1	0.096	12.8	65.1	11.5	28.1	66.3	0.63 ± 0.02	0.774	0.81 ± 0.06
									Mean age:	**0.91 ± 0.10**
RF16-13_1	1	0.036	7.93	13.8	31.3	11.2	44.3	0.58 ± 0.17	0.677	0.85 ± 0.26
RF16-13_2	1	0.002	0.67	0.49	0.10	0.8	51.0	0.48 ± 1.19	0.728	0.67 ± 1.63
RF16-13_3	1	0.112	12.5	25.7	29.7	18.5	52.6	1.11 ± 0.06	0.726	1.52 ± 0.13
RF16-13_4	1	0.018	3.19	6.52	24.88	4.7	58.1	0.69 ± 0.12	0.752	0.91 ± 0.17
									Mean age:	**0.99 ± 0.37**
RF16-16_1	1	0.514	122	124	13.7	151	52.3	0.63 ± 0.02	0.732	0.86 ± 0.07
RF16-16_2	1	0.747	149	165	21.2	188	45.8	0.74 ± 0.02	0.691	1.07 ± 0.09
RF16-16_3	1	0.545	112	179	9.26	154	49.5	0.66 ± 0.02	0.709	0.92 ± 0.07
RF16-16_4	1	0.399	88.4	91.1	11.0	110	58.1	0.67 ± 0.02	0.757	0.89 ± 0.07
RF16-16_5	1	0.518	102	123	20.1	131	45.3	0.73 ± 0.03	0.691	1.06 ± 0.09
									Mean age:	**0.96 ± 0.10**
RF16-18_2	1	0.049	15.7	30.4	23.8	22.9	36.3	0.39 ± 0.09	0.615	0.64 ± 0.16
RF16-18_4	1	0.157	22.5	59.2	14.7	36.4	47.3	0.80 ± 0.05	0.693	1.15 ± 0.10
RF16-18_5	1	0.150	35.2	12.7	15.6	38.1	41.7	0.73 ± 0.06	0.674	1.08 ± 0.12
RF16-18_6	3	1.160	198	280	41.5	264	53.5	0.81 ± 0.02	0.734	1.11 ± 0.08
RF16-18_7	4	0.567	79.1	75.7	79.1	96.9	51.9	1.08 ± 0.03	0.729	1.47 ± 0.11
									Mean age:	**1.09 ± 0.30**
RF16-21_1	1	0.295	72.5	164	16.3	111	51.9	0.49 ± 0.02	0.722	0.68 ± 0.05
RF16-21_2	1	0.055	19.8	22.4	73.2	25.0	52.3	0.40 ± 0.03	0.730	0.54 ± 0.05
RF16-21_3	1	0.049	17.4	12.7	51.7	20.3	49.7	0.44 ± 0.04	0.719	0.61 ± 0.07
RF16-21_4	1	0.998	86.4	79.7	46.2	105	43.4	1.75 ± 0.03	0.679	*2.58 ± 0.18*
RF16-21_5	1	0.053	23.8	39.0	43.5	33.0	44.0	0.29 ± 0.04	0.679	0.43 ± 0.06
									Mean age:	**0.57 ± 0.11**

(*continued*)

TABLE 2. APATITE (U-Th-Sm)/He DATA (*continued*)

Sample ID	*N*	^{4}He (nmol/g)	U (ppm)	Th (ppm)	Sm (ppm)	eU (ppm)	rs (μm)	Raw age (Ma)	Ft	Corrected age (Ma)
Yakutat block (*continued*)										
RF16-22_1	1	0.015	2.92	6.12	22.9	4.4	56.1	0.62 ± 0.17	0.743	0.83 ± 0.24
RF16-22_2	1	0.033	4.67	8.33	16.9	6.6	60.1	0.90 ± 0.10	0.758	1.18 ± 0.16
RF16-22_3	1	0.178	53.5	84.8	16.0	73.5	59.0	0.45 ± 0.01	0.755	0.59 ± 0.05
RF16-22_4	1	0.092	26.2	34.2	17.5	34.2	63.8	0.50 ± 0.02	0.777	0.64 ± 0.05
RF16-22_5	1	0.063	16.3	30.6	31.9	23.5	55.4	0.49 ± 0.03	0.738	0.66 ± 0.06
									Mean age:	**0.78 ± 0.24**
RF16-23_1	1	0.116	13.9	5.78	33.9	15.2	78.9	1.39 ± 0.02	0.821	1.68 ± 0.12
RF16-23_2	1	0.202	30.2	7.57	6.98	32.0	64.9	1.17 ± 0.03	0.785	1.49 ± 0.11
RF16-23_3	1	0.225	31.8	24.3	41.7	37.6	61.3	1.10 ± 0.03	0.770	1.42 ± 0.11
RF16-23_4	1	0.032	4.21	7.75	23.2	6.00	60.3	0.95 ± 0.08	0.761	1.24 ± 0.14
RF16-23_5	1	0.035	8.31	8.94	22.2	10.4	62.4	0.61 ± 0.05	0.772	*0.79 ± 0.09*
									Mean age:	**1.46 ± 0.18**
RF16-24_1	1	0.110	30.0	48.2	21.5	41.4	72.0	0.49 ± 0.01	0.800	0.61 ± 0.05
RF16-24_2	1	0.027	7.59	8.99	8.92	9.70	71.8	0.51 ± 0.03	0.801	0.63 ± 0.05
RF16-24_3	1	0.080	12.2	21.7	49.8	17.3	61.0	0.84 ± 0.03	0.763	1.09 ± 0.09
RF16-24_4	1	0.023	3.36	8.73	19.4	5.40	50.4	0.76 ± 0.17	0.713	1.06 ± 0.24
RF16-24_5	1	0.083	30.5	19.8	13.2	35.1	56.2	0.44 ± 0.02	0.753	0.58 ± 0.05
									Mean age:	**0.79 ± 0.26**
RF16-25_1	1	1.762	354	233	29.3	409	44.3	0.8 ± 0.01	0.688	1.16 ± 0.08
RF16-25_2	1	0.048	12.8	21.5	7.02	17.8	56.0	0.50 ± 0.03	0.744	0.67 ± 0.07
RF16-25_3	1	0.207	35.5	63.8	10.6	50.5	57.3	0.76 ± 0.02	0.750	1.01 ± 0.07
RF16-25_4	1	0.064	8.61	19.8	42.2	13.3	59.8	0.88 ± 0.04	0.757	1.15 ± 0.09
RF16-25_5	1	0.104	18.2	37.9	34.2	27.1	49.4	0.70 ± 0.04	0.710	0.98 ± 0.08
									Mean age:	**0.99 ± 0.20**
Boundary block										
RF16-32_2	1	0.100	18.1	12.2	27.9	21.0	33.3	0.87 ± 0.2	0.589	1.47 ± 0.34
RF16-32_3	1	0.096	19.6	8.65	32.5	21.7	30.3	0.81 ± 0.2	0.551	1.47 ± 0.45
RF16-32_4	1	0.761	27.6	12.6	54.7	30.6	36.5	4.54 ± 0.2	0.622	*7.26 ± 1.10*
RF16-32_5	1	0.018	1.02	1.91	0.58	1.50	30.4	2.08 ± 2.4	0.543	*4.08 ± 4.57*
									Mean age:	**1.47 ± 0.01**
RF16-30_1	1	0.491	36.5	11.7	51.6	39.3	45.4	2.29 ± 0.06	0.696	3.28 ± 0.24
RF16-30_2	1	0.167	19.4	11.5	40.2	22.0	42.6	1.39 ± 0.09	0.678	2.04 ± 0.20
RF16-30_3	1	0.110	18.6	8.57	42.4	20.7	40.7	0.97 ± 0.07	0.660	1.46 ± 0.17
RF16-30_5	1	0.457	39.1	6.25	75.5	40.6	51.8	2.06 ± 0.06	0.736	2.79 ± 0.21
									Mean age:	**2.39 ± 0.80**
RF16-04_1	1	0.365	17.1	21.1	21.4	22.1	50.0	3.04 ± 0.12	0.719	*4.22 ± 0.33*
RF16-04_2	1	0.652	70.6	34.6	16.4	78.7	52.1	1.54 ± 0.03	0.734	2.09 ± 0.15
RF16-04_3	1	0.172	11.0	15.7	18.7	14.7	66.2	2.15 ± 0.08	0.784	2.73 ± 0.21
RF16-04_4	1	0.440	17.8	18.9	22.1	22.3	62.5	3.63 ± 0.10	0.773	*4.69 ± 0.36*
RF16-04_5	1	0.608	51.2	8.22	18.7	53.1	57.2	2.12 ± 0.06	0.760	2.79 ± 0.21
									Mean age:	**2.54 ± 0.39**
RF16-27_1	1	0.274	24.2	30.2	12.7	31.3	50.9	1.62 ± 0.05	0.725	2.23 ± 0.17
RF16-27_2	1	0.308	31.0	51.6	22.6	43.1	50.7	1.32 ± 0.05	0.719	1.83 ± 0.14
RF16-27_3	1	0.110	8.59	9.09	10.3	10.7	52.4	1.88 ± 0.11	0.730	2.57 ± 0.23
RF16-27_5	1	0.126	8.82	5.04	1.74	10.0	44.6	2.33 ± 0.16	0.693	3.36 ± 0.32
									Mean age:	**2.50 ± 0.65**
Fairweather fault zone										
RF16-07_5	1	0.002	2.62	1.20	2.84	2.90	59.6	0.14 ± 0.19	0.768	*0.18 ± 0.24*
RF16-07_6	3	0.035	12.1	4.25	13.7	13.1	46.8	0.49 ± 0.14	0.706	0.70 ± 0.20
RF16-07_7	3	0.039	11.5	2.02	7.92	12.0	46.4	0.61 ± 0.12	0.706	0.86 ± 0.17
RF16-07_8	3	0.104	8.46	2.60	3.67	9.10	41.5	2.12 ± 0.28	0.670	*3.16 ± 0.46*
									Mean age:	**0.78 ± 0.11**
RF16-09_2	1	0.005	4.61	0.92	1.49	4.80	41.8	0.21 ± 0.32	0.677	0.31 ± 0.49
RF16-09_4	3	0.040	16.1	1.99	5.17	16.5	35.7	0.45 ± 0.17	0.620	0.72 ± 0.28
RF16-09_5	2	0.032	3.98	27.2	4.58	10.4	31.3	0.57 ± 0.55	0.522	1.09 ± 0.99
									Mean age:	**0.71 ± 0.39**

Note: *N*—number of grains, Ft—alpha ejection correction factor calculated using the method of Farley (2002), rs—spherical radius, eU—the effective uranium. Errors are 1σ uncertainties. Ages are mean age and standard deviation. Ages in italics were excluded from mean age.

TABLE 3. ZIRCON (U-Th)/He DATA

Sample ID	*N*	^{4}He (nmol/g)	U (ppm)	Th (ppm)	eU (ppm)	rs (μm)	Raw age (Ma)	Ft	Corrected age (Ma)
Yakutat block									
YB16-01_1	1	4.90	205	74.6	222	51.2	4.09 ± 0.1	0.779	5.24 ± 0.37
YB16-01_2	1	29.6	1600	193	1645	46.0	3.34 ± 0.1	0.758	4.41 ± 0.32
YB16-01_3	1	2.93	231	85.6	251	49.0	2.17 ± 0.1	0.770	2.81 ± 0.20
								Mean age:	**4.15 ± 1.23**
YB16-06_1	1	23.3	150	22.8	156	64.2	27.7 ± 0.8	0.823	33.6 ± 2.54
YB16-06_2	1	1.01	43.6	14.4	47.0	59.2	3.97 ± 0.1	0.808	4.91 ± 0.35
YB16-06_3	1	39.6	979	216	1030	50.9	7.13 ± 0.1	0.779	9.15 ± 0.66
YB16-06_4	1	18.8	550	133	581	47.4	6.01 ± 0.1	0.764	7.87 ± 0.56
RF16-11_1	1	129	900	301	971	70.2	24.6 ± 0.4	0.837	29.4 ± 2.10
RF16-11_2	1	60.5	376	55.5	389	61.9	28.8 ± 0.4	0.818	35.2 ± 2.51
RF16-11_3	1	100	599	53.4	611	59.9	30.3 ± 0.5	0.811	37.4 ± 2.70
RF16-13_1	1	22.6	177	68.4	193	56.1	21.7 ± 0.4	0.799	27.2 ± 1.94
RF16-13_2	1	80.9	362	132	393	54.5	38.1 ± 0.6	0.792	48.1 ± 3.39
RF16-13_3	1	115	468	220	520	60.5	40.9 ± 0.6	0.811	50.4 ± 3.54
RF16-21_1	1	65.3	577	225	629	53.5	19.2 ± 0.3	0.788	24.4 ± 1.74
RF16-21_2	1	103	636	68.9	653	64.4	29.3 ± 0.4	0.824	35.5 ± 2.55
RF16-21_3	1	240	1589	292	1658	58.7	26.8 ± 0.4	0.807	33.1 ± 2.37
RF16-22_1	1	17.9	129	52.7	142	65.5	23.4 ± 0.6	0.825	28.3 ± 2.09
RF16-22_2	1	39.9	269	114	296	64.3	24.9 ± 0.5	0.822	30.3 ± 2.20
RF16-22_3	1	29.1	131	42.5	141	63.1	38.3 ± 0.6	0.819	46.7 ± 3.32
RF16-25_1	1	169	970	294	1039	57.6	30.2 ± 0.4	0.803	37.6 ± 2.70
RF16-25_2	1	201	759	90.2	780	65.4	47.6 ± 0.9	0.827	57.5 ± 4.23
RF16-25_3	1	148	692	270	755	58.6	36.3 ± 0.6	0.806	45.0 ± 3.19
Boundary block									
RF16-04_1	1	13.7	308	64.6	323	57.5	7.89 ± 0.1	0.803	9.81 ± 0.69
RF16-04_2	1	21.4	300	156	337	59.2	11.8 ± 0.2	0.807	14.6 ± 1.05
RF16-04_3	1	143	1455	129	1485	52.8	17.9 ± 0.3	0.788	22.7 ± 1.64
RF16-27_1	1	6.89	294	69.9	310	71.7	4.12 ± 0.1	0.841	4.89 ± 0.35
RF16-27_2	1	11.9	165	53.7	178	71.7	12.5 ± 0.2	0.840	14.8 ± 1.07
RF16-27_3	1	31.9	644	178	685	62.4	8.63 ± 0.1	0.818	10.6 ± 0.75
RF16-30_1	1	199	4057	462	4166	41.5	8.85 ± 0.2	0.735	12.0 ± 0.89
RF16-30_2	1	211	4577	575	4712	38.3	8.29 ± 0.1	0.712	11.6 ± 0.84
RF16-30_3	1	182	2177	381	2266	40.5	14.9 ± 0.2	0.726	20.5 ± 1.46
Fairweather fault zone									
		He (mol)	U (ng)	Th (ng)					
YAKB58_1	1	6.418E-16	0.21	0.048		71.3	0.54 ± 0.1	0.820	0.66± 0.05
YAKB58_2	1	1.310E-15	0.28	0.057		75.9	0.82 ± 0.1	0.832	0.99± 0.07
YAKB58_3	1	8.089E-16	0.29	0.110		66.8	0.48 ± 0.1	0.807	0.59± 0.04
								Mean age:	**0.75± 0.21**

Note: *N*—number of grains, Ft—alpha ejection correction factor calculated using the method of Farley (2002), rs—spherical radius, eU—the effective uranium. Errors are 1σ uncertainties. Ages are mean age and standard deviation.

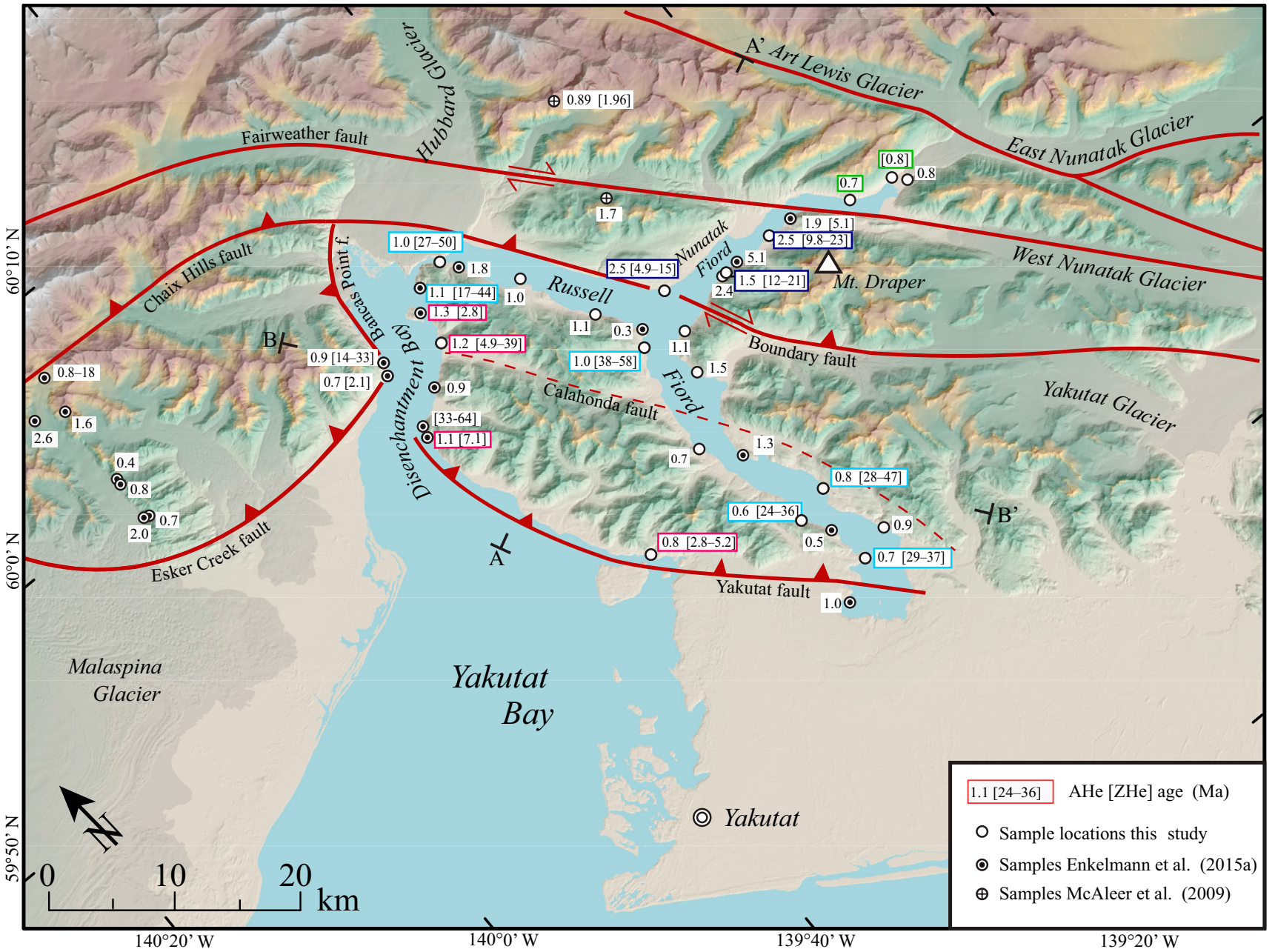

Figure 3. Topography and principal geologic structures of the study area. New and previously published apatite (U-Th-Sm)/He (AHe) and zircon (U-Th)/He (ZHe) data are shown. In general, the mean age is recorded for each sample. For zircons, the mean age is displayed for those samples that reproduced well, but for most samples, the range of single-grain ages is displayed. Sample labels with a colored frame indicate samples used for time-temperature (*t-T*) path modeling shown in Figure 4. Locations for two swath profiles are indicated by A–A' and B–B' (see Fig. 5). Present-day glacial coverage is from GLIMS (Raup et al., 2007), and elevation data are from the Advanced Spaceborne Thermal Emission and Reflection Radiometer Global Digital Elevation Model (ASTER GDEM) version 2, a product of the Ministry of Economy, Trade and Industry (METI, Japan) and the National Aeronautics and Space Administration (NASA).

paths) supported by our AHe and ZHe ages (inverse mode of the HeFTy software, v 1.9.1; Ketcham, 2005). For each sample, at least 50,000 random *t-T* paths were generated, and modeled AHe and ZHe ages were calculated. The modeled data were then compared with the measured input data. We used the Kolmogorov-Smirnov (K-S) test to evaluate if the modeled data agreed within statistical limits with the measured data. The *t-T* path was selected and recorded as a good- or acceptable-fit solution, or the path was discarded. At least two *t-T* constraints (constraint windows) were set to guide inverse modeling. The first constraint window was set at the beginning of the thermal history, predating the oldest single-grain age of the sample and allowing a wide temperature range that exceeded the helium retention temperature window for zircon (150–220 °C; Reiners, 2005). The final constraint was set at the present-day surface temperature of 0–10 °C. Where we had apatite and zircon data, we set another *t-T* constraint window that ranged from the oldest to younger than the youngest AHe age of the sample and temperatures that covered the entire AHe diffusion temperature range (50–120 °C; Flowers et al., 2009).

For modeling, we included all aliquot ages, which in some samples was up to seven helium models per sample—the upper limit in the HeFTy program. We used the radiation damage and accumulation models for helium diffusion in apatite (Flowers et al., 2009) and zircon (Guenthner et al., 2013). To accommodate the large intrasample dispersion, particularly for the ZHe data, we applied a 15%–35% error of the single-grain ages to allow the software to find possible *t-T* solutions (R. Ketcham, 2017, personal commun. with Enkelmann). Such an error represents the actual precision of the (U-Th-Sm)/He method because it is greatly influenced by external errors, including the alpha-ejection correction, heterogeneous chemistry, micro-inclusions and impurities, and other factors. Overall, this large external error is a realistic representation of the reproducibility of helium ages (cf. rapidly cooled samples in Tables 2 and 3). The model parameters and results for each individual sample are shown in the Data Repository material (Table S1; Fig. S3), and compiled plots of good- and acceptable-fit model results of samples from specific structurally bound tectonic panels are presented in Figure 4. We also conducted thermal history modeling of samples with previously published AHe and ZHe data from the study area that have not been modeled before (Enkelmann et al., 2015a).

Thermal History Model Results

The *t-T* models revealed different cooling histories for the Boundary block and the Russell Fiord block. The Russell Fiord block reveals two distinct thermal histories that necessitate a tectonic break in the block (Figs. 4A and 4B). Samples located near the Yakutat fault and Disenchantment Bay (YB16–01, YB16–06, YA47, YA52) reveal rapid cooling from 160 °C to 70 °C starting between 12 and 6 Ma and these samples show an increase in cooling (65 ± 5 °C/m.y.) from 70 °C to surface temperatures since 1 Ma (Fig. 4B). In contrast, samples located farther away from the Yakutat fault reveal very slow cooling from 160 °C to 80 °C starting 60–40 Ma and lasting until very recently. This long period of steady state was followed by very rapid cooling (65 ± 5 °C/m.y.) from 70 °C to surface temperatures starting 1 Ma (Fig. 4A).

The Boundary block samples reveal two phases of cooling. The beginning of the first phase is less well defined, but it ranges in age between 15 Ma and 7 Ma (in samples RF16–04, RF16–27, RF16–30) and resulted in cooling from 160 °C to 60 °C by 2.5 Ma (Fig. 4C). This phase was followed by cooling with increased rates (22 ± 2 °C/m.y.) from 60 °C to surface temperatures today. These results for the two blocks mean that the Boundary block and the Russell Fiord block have had different cooling histories since the Miocene. The Boundary block cooled from greater temperatures/depths (>160 °C; Fig. 4C) than the Russell Fiord block, which reveals that most rocks were already at shallow depths with temperatures of <160 °C (Fig. 4A). The Pleistocene cooling started earlier in the Boundary block (ca. 2.5 Ma) than in the Russell Fiord block (ca. 1 Ma), but with lower rates. Samples from the Fairweather fault zone reveal exceptionally rapid cooling (160 ± 10 °C/m.y.) from temperatures of >160 °C to the surface temperature within the last 0.8 m.y. (Fig. 4D).

DISCUSSION

Spatial and Temporal Patterns of Rock Exhumation

Thermal history modeling clearly shows that the three fault-bound blocks experienced different cooling and inferred exhumation histories (Fig. 4). To explore spatial variations in rock cooling and exhumation across the crustal blocks bounded by the Yakutat, Boundary, and Fairweather faults, we present our new AHe and ZHe data together with previously published data in map view (Fig. 3) and on cross-sectional swath profiles (Fig. 5). Because all samples were collected at sea level, we can exclude spatial variations in the thermochronometric data due to sample elevation, and thus we infer that the pattern of rock cooling is due to a combination of structural position and erosional exhumation. We find distinct differences in cooling and exhumation between the fault-bounded blocks.

To aid our interpretation, we also examined detrital apatite fission-track (AFT) and zircon fission-track (ZFT) data from modern sand in rivers and glaciers in the study region (Fig. 6) from Falkowski et al. (2014) and Enkelmann et al. (2015b). Dating detrital minerals requires the single-grain analysis of ~100 grains to obtain an age distribution that represents the integrated thermochronometric age signal of the entire catchment. In this analysis, binomial peak fitting was used to find age components that best fit the measured grain-age distribution (Fig. 6; Brandon, 1996). In general, the fission-track systems are sensitive to slightly higher temperature than the (U-Th-Sm)/He systems. For apatite, the closure temperature ranges between 120 °C and 100 °C (Green et al., 1986), and for zircon, it ranges between 300 °C and 200 °C (Brandon et al., 1998; Rahn et al., 2004). These temperatures are typical at 3–5.5 km (AFT) and 9.5–14.5 km (ZFT) assuming a 25 ± 5 °C/km geothermal gradient and 10 °C surface temperature. Thus, the AFT system provides information about cooling between the temperature windows of the AHe and ZHe systems, and the ZFT data provide information about heating and cooling at relatively high temperatures.

Cooling History of the Russell Fiord Block

To a first order, the AHe and ZHe ages in the Russell Fiord block become progressively older with increasing distance from the Yakutat fault (Fig. 3), a pattern that would be expected from the hanging wall of a reverse fault (Ehlers and Farley, 2003; Lock and Willett, 2008; Enkelmann et al., 2015a). Rocks in the hanging wall just above the reverse fault originate from the deepest structural level and cool more rapidly in comparison to rocks farther away from the fault, which typically represent material exhumed from shallower depths (e.g., Ehlers and Farley, 2003). The AHe ages increase from ca. 0.5 Ma near the Yakutat fault to ca. 1.1–1.5 Ma farther away (Fig. 3), indicating that all rocks were exhumed very recently from depths below the helium PRZ for apatite (>80 °C). The spatial trend in AHe ages is obscured and not well developed when projected onto the swath profile, but the ZHe ages show a distinct pattern with ages that range from 7 to 3 Ma near the Yakutat fault and from 64 to 17 Ma away from the fault (Fig. 5A). ZHe ages from samples collected near the Yakutat fault suggest that those rocks were exhumed recently from depths below the helium PRZ for zircon (>180 °C), but that the

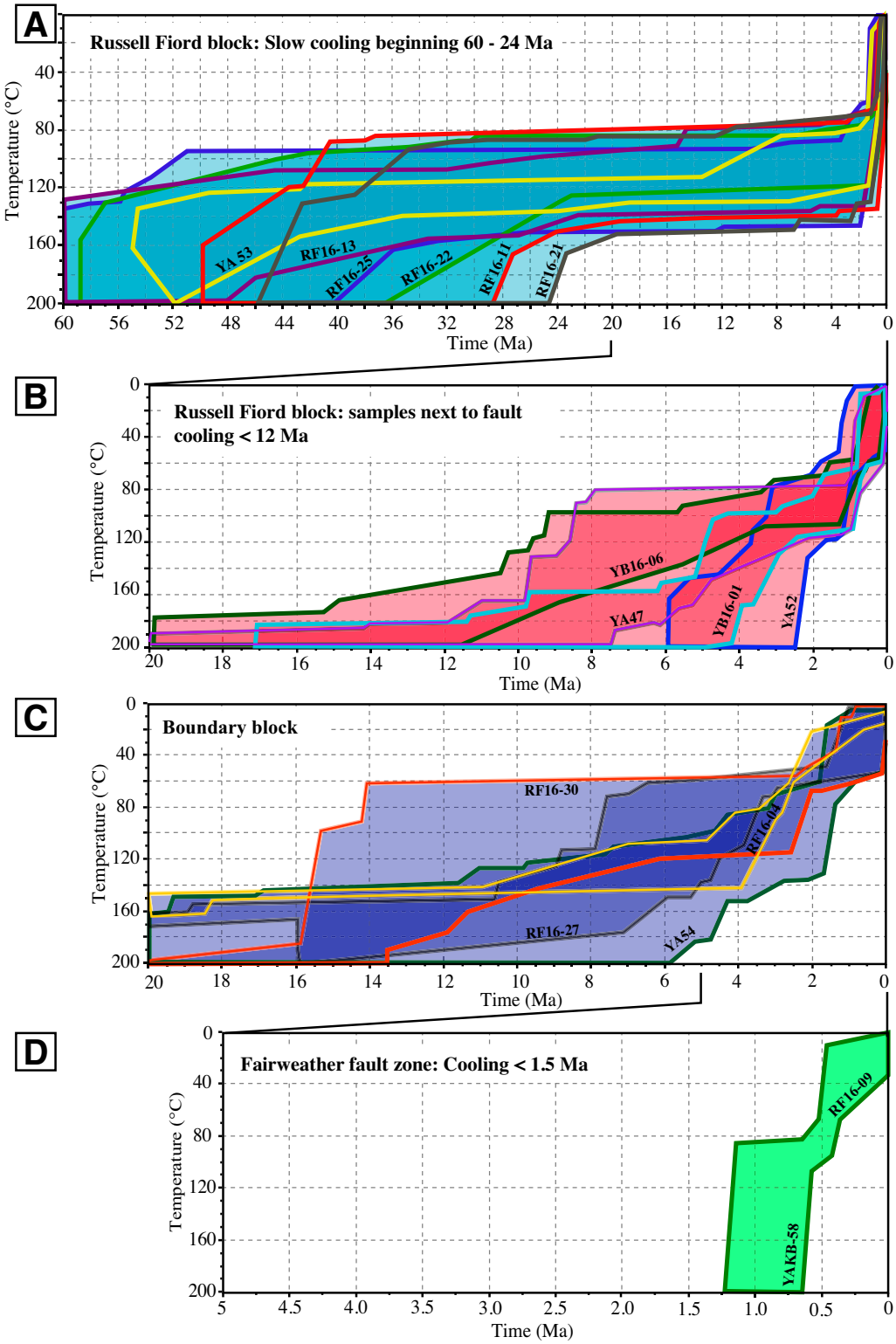

Figure 4. Compiled time-temperature (*t-T*) models of specific fault-bounded regions. (A) Samples from the Russell Fiord block with zircon ages that show a wide age spread. (B) Samples from the Russell Fiord block with young zircon ages. (C) Samples from the Boundary block. (D) Samples from the Fairweather fault zone. All models include apatite and zircon U-Th/He ages, constraining possible thermal histories between 200 °C and 50 °C. Shown are envelopes of good-fit solutions for each sample (outlined with different colors), but a few samples yielded only acceptable-fit solutions. Darker-shaded areas indicate regions where two or more models generated overlapping time-temperature paths. Note the different age ranges for the different plots. For model D, zircon single-grain data were used from YAKB-58 and apatite single-grain data were used from RF16–09. Model results for individual samples are shown in the Data Repository material (Figure S3).

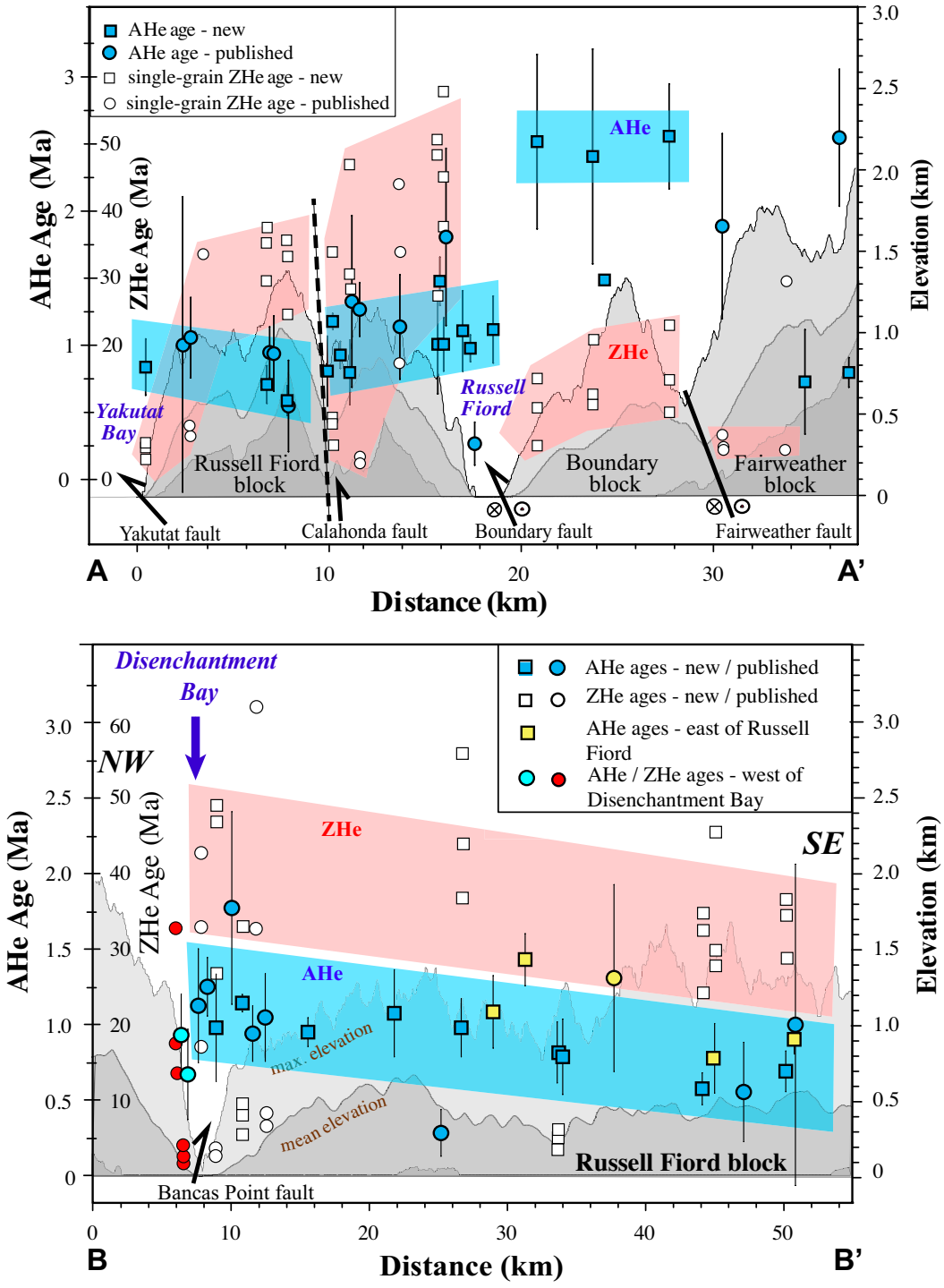

Figure 5. Swath profiles and plotted apatite (U-Th-Sm)/He (AHe) and zircon (U-Th)/He (ZHe) ages of this study and those previously published. See Figure 3 for the location of profile A–A', which crosses normal to the strike of the Yakutat, Boundary, and Fairweather faults, and profile B–B', which crosses Disenchantment Bay and the south end of Russell Fiord. Note the different age scale for the apatite and zircon data on the left *y* axis. Blue and red shaded areas indicate the general age trends of AHe and ZHe data, respectively.

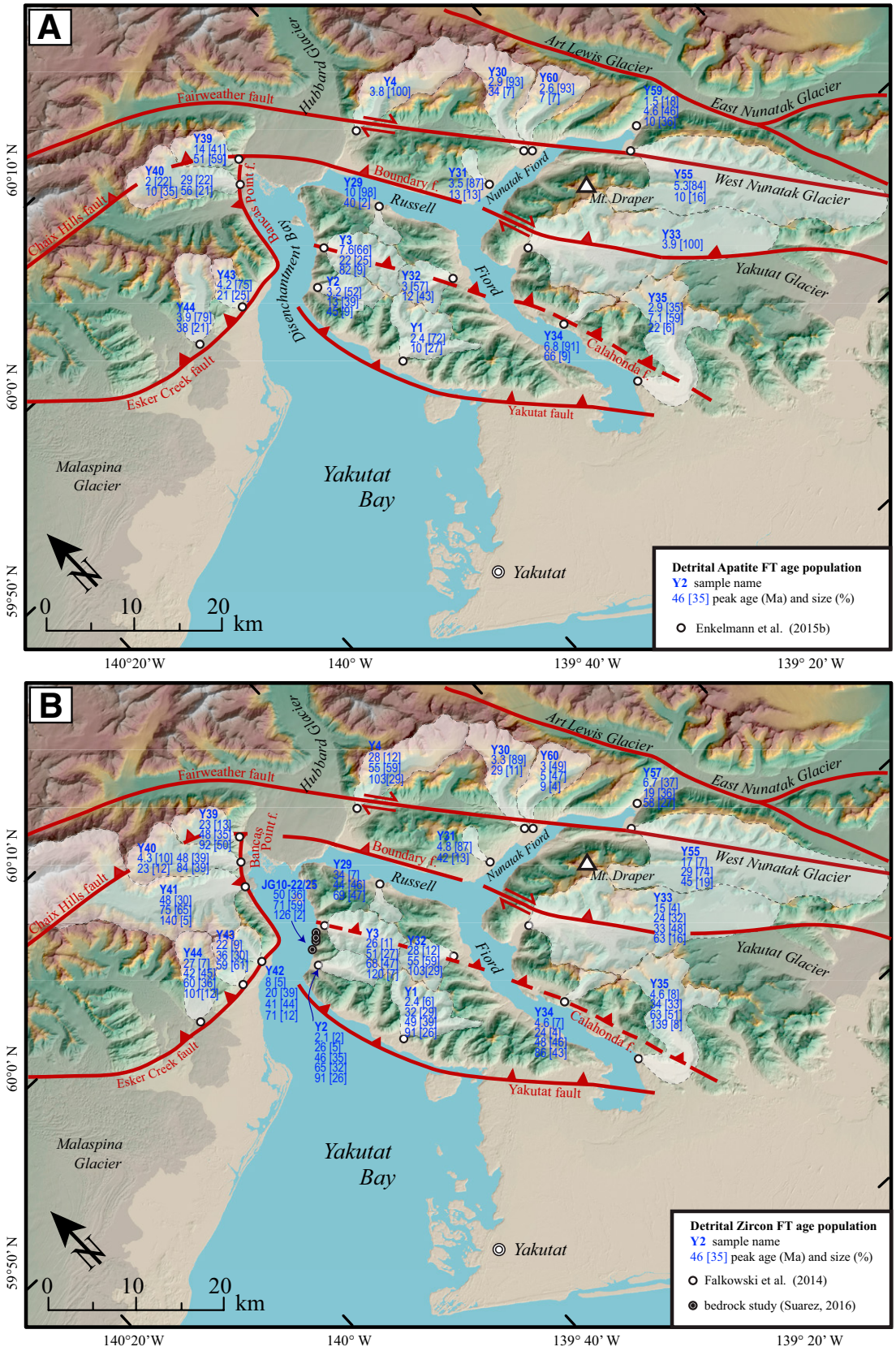

Figure 6. Peak-fitting results of the detrital apatite (A) and zircon (B) fission-track (FT) ages from modern sand. Catchments of samples are outlined in white and are transparent. Combined zircon fission-track peak-fitting results of four bedrock samples collected along the eastern side of Disenchantment Bay are shown in B; f.—fault.

rocks structurally above resided within the PRZ prior to the late Miocene to Holocene exhumation, resulting in a wide range of ZHe ages between sample aliquots. The fact that all samples yielded single-grain ages that postdate the Late Cretaceous–Paleocene deposition age of the Yakutat Group (Garver and Davidson, 2017; Sophis et al., 2017) suggests thermal resetting by burial and heating to at least 180–200 °C. This interpretation is supported by the *t-T* path models, suggesting for most samples a long residence time within the ZHe PRZ followed by rapid cooling from >80 °C since ca. 1 Ma (Fig. 4A).

Four samples located near the fault trace reveal a different thermal history that suggests moderate cooling rates since the late Miocene from ~200 °C followed by an increase in the rate of cooling since ca. 1 Ma (Fig. 4B). Support for this interpretation comes from the observed spatial trend in detrital fission-track data of fluvial deposits from catchments draining the Russell Fiord block (Fig. 6). The detrital thermochronology age distribution represents the cooling signal integrated over an entire catchment and is influenced by many factors, such as the age variations due to topography, varying apatite yield of different lithologies, spatial variations in erosion, catchment hypsometry, and other factors (e.g., Stock et al., 2006; Ehlers et al., 2015). The youngest detrital age component signifies the most rapidly cooled rocks in the catchment, which is likely to be those at the lowest elevations, or those close to the faults. Therefore, the youngest age populations can be used for comparison to our bedrock data collected at sea level. With this approach, the age components and their relative size may provide information about a larger area of the Russell Fiord block that was not sampled by bedrock analysis, which was limited to collection at sea level. The detrital data show that the Russell Fiord block is tilted, with younger cooling ages, and thus probably more exhumation, to the SW, near the Yakutat fault. The catchment located closest to the Yakutat fault (Y1) yielded an AFT age population at 2.4 ± 0.3 Ma, composed of 72% of all grains, and the remaining grains defined a population at 10 ± 1.8 Ma (Fig. 6A; Enkelmann et al., 2015b). Catchments located farther away from the Yakutat fault (Y2 and Y32) yielded AFT age components slightly older with peaks at 3.2 ± 0.7 Ma (52%) and 3.0 ± 0.7 Ma (57%). Finally, the catchment farthest away from the fault (draining into Russell Fiord, Y29) had the youngest age population at 9.6 ± 2.0 Ma (98%; Fig. 6A). A late Miocene (ca. 12–6 Ma) start to increased cooling below ~200–180 °C is suggested based on the AHe and ZHe data used for *t-T* path modeling of samples close to the Yakutat fault (Fig. 4B). Interestingly, all seven catchments draining the Russell Fiord block yielded an age component with AFT grain-age populations ranging between 13 and 6 Ma and composing >50% of the sample grains (Fig. 6A). These results indicate widespread late Miocene cooling below ~100 °C for most of the Russell Fiord block. This time correlates with the end of the Poul Creek Formation deposition and the beginning of the deposition of the Yakataga Formation. The boundary between these two formations is not well determined, and our data may suggest a slight uplift and formation of an unconformity during its transport along the North American margin.

The ZFT closure temperature of 300–200 °C is above the ZHe system (Reiners and Brandon, 2006). Recall that most ZHe ages indicate slow cooling from the helium PRZ (~180 ± 20 °C), and inverse modeling indicates a long residence time in that temperature window. Thus, we would expect that the detrital ZFT ages also would record slow pre-Miocene cooling of the Russell Fiord block. Except for two catchments (Y1 and Y2), the youngest ZFT age populations in the Russell Fiord block are Oligocene, and they range between 34 and 24 Ma and constitute 1%–33% of the sample (Fig. 6B). Catchments Y1 and Y2 yielded age components that peak at 2.4 ± 0.3 Ma and 2.1 ± 0.6 Ma but comprise only 6% and 2% of all grains, respectively. These very young grains probably originated from the vicinity of the Yakutat fault, where rapid fault slip causes isotherm compression due to the upward advection of heat, which may have caused cooling from >300 °C sufficient to be recorded in the ZFT system (Enkelmann et al., 2015a).

As expected, most ZFT detrital age populations are not reset by the young tectonic setting. Most detrital ZFT age populations are primarily in the Eocene at 55–45 Ma and also in Late Cretaceous to early Paleocene at 100–60 Ma (Fig. 6B). These data are in agreement with the ZFT age distributions in the four bedrock samples of sandstones collected along the eastern shore of Disenchantment Bay (Fig. 6B). The combined results of all 205 grains from the four samples revealed two main age populations with peaks at 49.5 ± 2.85 Ma (33%) and 70.8 ± 3.7 Ma (59%), and a very small Early Cretaceous (ca. 125 Ma) age component (Suarez, 2016). Taken together, all ZFT data from the Russell Fiord block yielded age components that predate and postdate sediment deposition of the Yakutat Group and thus indicate partial thermal resetting. Thus, after deposition in the Maastrichtian to Paleocene (72–60 Ma detrital zircon U-Pb ages; see Sophis et al., 2017), rocks were quickly buried and heated and subsequently experienced a cooling at ca. 50 Ma. This early Eocene cooling may have been related to uplift and exhumation associated with the overthrusting of the Yakutat Group rocks over Eocene basalts on the Dangerous River fault during the collision of the Yakutat microplate with the western margin of North America farther south (i.e., Garver and Davidson, 2017).

The ZHe age pattern also reveals an important tectonic break across the Russell Fiord block. In the swath profile (A–A′), ZHe ages increase with increasing distance from the Yakutat fault, and there is also an increase in the spread of ages in single-grain aliquots from each sample (Fig. 5A). This pattern is repeated again starting ~10 km northeast from the Yakutat fault (Figs. 3 and 5A), where the ZHe ages are young and reproduce fairly well. This pattern can be explained by the existence of a previously unrecognized fault parallel to the Yakutat fault, and in this case, the young ZHe ages would be on the hanging wall, adjacent to the fault. The AHe age pattern also shows an offset (Fig. 5A).

The position of this new inferred fault is revealed in the digital elevation model (DEM), which reveals elongated valleys and lineaments in the topography (Fig. 3). The DEM clearly shows the location of the Fairweather, Boundary, and Yakutat faults, which are located in low-relief regions that form long valleys (Fig. 3). The map also reveals a distinct northwest-southeast linear trend in the topography with two oppositely draining straight valleys suggesting the existence of this inferred fault (dashed line in Fig. 3). Thus, based on the young ZHe and AHe pattern of offset ages, and the distinctive topography, we suggest that the simplest explanation is a splay fault that parallels the Boundary and Yakutat faults. We refer to this as the "Calahonda fault" after the Calahonda River, which follows the fault on the Yakutat peninsula and flows into Disenchantment Bay (Fig. 3). The offset in ages is most evident in the ZHe ages, suggesting that rocks northeast of the fault were exhumed from greater depths than those to the southwest. Based on the age pattern, the neighboring structures, and the general tectonic setting, this structure is inferred to be a northeast-dipping reverse fault that crosses the peninsula of the Russell Fiord block and probably continues southeast of the southern arm of Russell Fiord. Along the southeast arm of Russell Fiord, a small (6%–7%), but very young detrital ZFT age population with peaks at 4.6 Ma occurs in the two catchments (Y34 and Y35) that sit on the north side of the proposed fault (Fig. 6B). Recall that the detrital ZFT age populations just north of the Yakutat fault of 2.4 Ma may indicate that the new proposed structure formed earlier than the Yakutat fault. Future work should target samples of bedrock just above (north of) the Calahonda fault trace in the area of Russell Fiord. The complicated structure of the flysch and mélange lithologies of the Yakutat Group combined with the remoteness, dense

vegetation, and unconsolidated sediment cover most likely explain why this fault had not been mapped.

The Russell Fiord block rocks experienced maximum heating at ca. 50 Ma, followed by slow cooling until the late Miocene, when the Yakutat fault was initiated. The structurally deepest rocks were exhumed just north of the Yakutat fault and north of the Calahonda fault, which parallels the Yakutat fault for 40 km. These deepest exhumed rocks originated from temperatures of ~200–300 °C, corresponding to 9.5–14.5 km depths (assuming a geothermal gradient of 25 ± 5 ºC/km and ~10 °C surface temperature). However, most rocks were exhumed from shallower depths corresponding to the ZHe PRZ of 160–200 °C. Models of the thermal history indicate late Miocene cooling from ~180 °C to below 70 °C with inferred exhumation rates of 0.4–1.1 km/m.y. that lasted until ca. 1 Ma, when the exhumation increased to rates of ~2.4–3 km/m.y. Pleistocene cooling is recorded in all samples of the Russell Fiord block, suggesting at least 2–3 km of exhumation since 1 Ma.

Cooling History of the Boundary Block

The Boundary block has different lithologies and a higher metamorphic grade compared to the Russell Fiord block (Fig. 2), and the low-temperature cooling history is different (Fig. 4C). AHe ages from the Boundary block are older (ca. 2.5 Ma) and display no obvious correlation with distance from either the Boundary or the Fairweather faults (Fig. 5A). However, the ZHe ages increase with increasing distance from the Boundary fault (Fig. 5A). In general, the ZHe ages are relatively young (between 23 and 5 Ma) and show low age dispersion (Table 2). Previous thermochronometric dating in the Boundary block is limited. Along Nunatak Fiord, a mean AHe age of 5.1 ± 2.8 Ma (Enkelmann et al., 2015a) and a mean AHe age of 1.67 ± 0.12 Ma were reported for a tonalite sample at 900 m of elevation west of the fiord (McAleer et al., 2009). Thermal history modeling of the three samples in this study that have both AHe and ZHe data (RF16–27, RF16–30, RF16–04) reveals two distinct periods of cooling. Cooling started in the Miocene between 15 Ma and 7 Ma and progressed from 160 °C to 60 °C until 4–3 Ma, and then more rapid cooling occurred through ~60 °C to surface temperatures in the last 2 m.y. (Fig. 4C). A comparison of these new bedrock ages to published detrital fission-track data from the Boundary block provides important insight into the history of this block. One small catchment (Y31) exclusively drains the Boundary block, and in this sample, 87% of apatite grains compose a fission-track age population at 3.5 Ma (Enkelmann et al., 2015b), and 87% of the zircon grains from the same sample compose an age population at 4.8 Ma (Fig. 6; Falkowski et al., 2014). Two other detrital samples cover parts of the Boundary block east of Nunatak Fiord. The interpretation of the cooling signal is less obvious for these two samples because they are derived from very large catchments that include the Russell Fiord and Boundary blocks (Y33), and the Boundary block, Fairweather fault zone, and Chugach terrane (Y55). However, the catchment of sample Y33 is mostly underlain by the Boundary block, and this sample has a single AFT age component at 3.9 Ma (100%; Fig. 6A).

Thus, the Boundary block has a rapid cooling history that is distinct from adjacent blocks. The narrow age range between the AFT and ZFT and (U-Th-Sm)/He systems is expected if exhumation was very rapid between ca. 5 Ma and ca. 2 Ma. This result indicates cooling from 300 °C to below 60 °C with rates of 80–120 °C/m.y. and inferred exhumation rates of 2.7–6 km/m.y. (assuming a geothermal gradient of 25 ± 5 °C/km). However, the AHe ages suggest only moderate cooling rates of ~30 °C/m.y. since ca. 2 Ma, and we therefore infer the Boundary block is no longer exhuming at such high rates. The *t-T* path model is not constrained for temperatures below the PRZ (~40 °C), and thus a wide range of possible *t-T* path solutions is shown in the model results. The fact that almost all detrital ZFT ages from one catchment (Y31) record Pliocene cooling suggests that the total amount of exhumation of the Boundary block is much larger compared to that of the Russell Fiord block. This result is in agreement with the observed higher metamorphic grade of sedimentary rocks and the exposed intrusive rocks, which indicate at least 8–12 km of exhumation since the Pliocene.

Cooling History of the Fairweather Fault Zone

We sampled the fine-grained, well-foliated amphibolites exposed at the northeastern end of Nunatak Fiord. These rocks are part of the Chugach metamorphic complex, a 7-km-wide sliver between the Fairweather fault (active Yakutat–North America plate boundary) and the Border Ranges fault (suture between the Chugach terrane and Insular terrane). The Fairweather fault zone itself is a >1-km-wide valley occupied by the West Nunatak Glacier and heavy vegetation and glacial deposits south and north of Nunatak Fiord, respectively (Fig. 2). These rocks had very low yield in apatite and zircon, and only two samples produced AHe ages, and another sample produced a ZHe age (Fig. 3; Tables 2 and 3). All three ages are ca. 0.8 Ma and are the same within error. Thermal history modeling suggests rapid cooling through the apatite closure temperature window starting at ca. 0.5 Ma at 100 °C until today at surface temperatures (Data Repository Fig. S3). We combined the AHe and ZHe data from two samples that are 1 km apart along the northern margin of Nunatak Fiord (samples YB16–09 and RF-58; Fig. 3) to model the combined thermal history of the area. The modeled *t-T* paths suggest cooling below 200 °C started between 1.2 and 0.6 Ma, suggesting an extreme cooling rate of 150–300 °C/m.y. in the Fairweather fault zone (Fig. 4D). There are no other thermochronometric data available for the fault zone itself, but detrital AFT and ZFT data were published from catchments that drain the thin Chugach block between the Border Ranges fault and the Fairweather fault. Catchments Y30 and Y60 are both underlain only by CMC rocks exposed north of Nunatak Fiord. Detrital AFT data reveal a peak at 2.9 Ma and 2.6 Ma in catchment Y30 and Y60, respectively, comprising 93% of all grains in each sample (Fig. 6A). Detrital ZFT data reveal an age population at 3.3 Ma (Y30) that makes up 89% of all grains in sample Y30, and two Pliocene age populations at 3 Ma (49%) and 5 Ma (47%) in sample Y60 (Fig. 6B). The catchment of sample Y4 is located 20 km farther northwest of Nunatak Fiord and yielded detrital AFT data that peak at 3.8 Ma (100%), suggesting slightly less rapid cooling. In contrast, the detrital ZFT ages in that catchment are much older, with the youngest peak at 28 Ma (12%). These older ages suggest that the rocks were already at shallow crustal depths when rapid Pliocene exhumation started.

Together, these data document extremely rapid exhumation rates (>5 km/m.y.) in the Pliocene, similar to those observed in the Boundary block that exhumed rocks from below the ZFT closure temperature. In contrast to the Boundary block, these rapid rates are ongoing, and exhumation has continued since at least 3 Ma. The timing of the beginning of these rapid rates is unclear, but it can be assumed to be long lasting due to the fact that the Fairweather fault constitutes the plate boundary. Such rapid exhumation on continental transform faults, such as the San Andreas and Alpine fault systems, has been recorded before (e.g., Spotila et al., 1998; Garver and Kamp, 2002; Little et al., 2005).

Tectonic Implications

Our thermochronologic analysis documents distinct and different cooling histories of fault-bounded blocks that parallel the northern end of the Fairweather transform boundary. These data have important implications for the tectonic configuration and traces of active faults in this boundary zone, but they also have implications for the long-term evolution of

tectonic blocks along this part of the Northern Cordillera in the Neogene. The Fairweather fault zone and rocks of the CMC experienced extremely rapid exhumation from depths of more than 8–12 km since at least mid-Pliocene time (3 Ma). In contrast, the rocks of the adjacent Boundary block were exhumed from similar depth and with similar high rates but beginning during the early Pliocene (ca. 5 Ma), followed by much lower exhumation rates since then. The outermost blocks west of the Boundary fault have a distinct thermal history compared to the adjacent Boundary block, and thus they may have different tectonic histories.

Dextral Translation of the Boundary Block

The rocks of the Boundary block share a metamorphic history and exhumation history that are similar to inboard rocks (CMC and the Baranof schist to the south) and different from outboard rocks of the Yakutat Group. Thus, the CMC and the metamorphic rocks of the Boundary block may be tectonically allied, but they are clearly separated by the dextral Fairweather fault. Offset between the two blocks may mean that the metamorphic rocks of the Boundary block experienced rapid Pliocene exhumation farther south, and they were then subsequently juxtaposed after dextral translation with the higher-metamorphic-grade CMC rocks. Assuming dextral displacement with a rate of 44–50 km/m.y. for the Boundary block with respect to North America (full coupling with Pacific plate), these rocks may have been located as far south as Baranof Island at 10–5 Ma. If this was the case, the rocks of the Boundary block (i.e., schist of Nunatak Fiord and Eocene plutons) may be allied to the schist of Baranof Island and the Crawfish pluton (Garver and Davidson, 2015). In this case, the Boundary block represents a sliver of the Chugach–Prince William terrane flysch intruded by plutons of the Sanak Baranof belt (Garver and Davidson, 2015, 2017; Davidson and Garver, 2017). It is possible that the rapid exhumation of the Boundary block rocks was driven by transpression and translation along the margin.

Even though the Fairweather fault is dominated by strike-slip displacement, the rapid exhumation rates from the thermochronologic data indicate significant vertical motion has occurred during slip. These cooling data imply that the Fairweather fault accommodates dip-slip motion by the Chugach metamorphic complex, which was exhumed in the hanging wall of a steeply northeast-dipping fault (Fig. 7A). This basic observation suggests that the juxtaposition of the previously rapidly exhuming Boundary block into the footwall position of the northern Fairweather fault led to the deceleration of the exhumation of the Boundary block at around 2.5–2 Ma. In contrast, exhumation rates are high in the CMC rocks that form the hanging wall at this location (Fig. 7A).

Active Faulting

The Fairweather strike-slip fault and the adjacent strands highlighted in this paper are part of an active tectonic plate boundary, and the connection and correlation of fault strands are important for a number of reasons. Based on GPS measurements, the Fairweather fault accommodates pure dextral strike-slip motion of 44 km/m.y. (Elliott et al., 2010). The M 7.9 Lituya Bay earthquake in 1958 resulted in a coseismic dextral displacement of at least 4 m along the entire 225 km length of the onshore Fairweather fault (Fig. 1; Miller, 1961; Tocher, 1960). Dextral slip has caused displacement of several glacial valleys that cross the Fairweather fault, and in our study area, this displacement is recognized by the 6 km offset of the eastern and western arms of Nunatak Fiord (Fig. 2).

The northern termination of the Fairweather fault is a complex series of fault segments in the area of the terminus of the Hubbard Glacier, and the fault is thought to bend 30° counterclockwise to connect with the Contact fault under the Seward ice field (Fig. 7B). Earthquake relocation studies (Doser, 2012) and ice-flow velocity studies (Ford et al., 2003) suggest complex structures under the Seward ice field and Mount St. Elias, including reverse, strike-slip, and normal faulting. Some of the Fairweather fault motion appears to be transferred farther inboard along the Connector fault, which continues with a NNW strike underneath the Hubbard Glacier (Fig. 7B; Doser, 2014). Field observations of these rocks are hampered by overlying ice, but detrital and bedrock thermochronologic studies reveal that extremely rapid exhumation rates (~5 km/m.y.) occurred in a localized area at the indenting Yakutat plate corner (syntaxis). The focused exhumation started at least 10 Ma northeast of the Connector fault and shifted south to the Hubbard and Seward ice fields ca. 5 Ma (Falkowski and Enkelmann, 2016; Enkelmann et al., 2017). Sometime after 2 Ma, focused rapid exhumation shifted south of the plate boundary along southward-directed reverse faults northwest of Disenchantment Bay (Fig. 7B; Enkelmann et al., 2015b).

Significant thrusting and coseismic uplift occur along these strike-slip fault strands in this tectonic corner. The Boundary fault separates the Boundary block from the Russell Fiord block, and it has been long recognized as an important fault between uplifted metamorphic rocks and strata of the Yakutat Group (Tarr and Butler, 1909). The M 8.1 Yakutat Bay earthquake in 1899 (Fig. 7B) caused ~1.5 m of coseismic uplift along the western shoreline of the Boundary block, interpreted as reverse slip along a northeast-dipping fault (Tarr and Martin, 1912; Plafker and Thatcher, 2008). The relative block motion model of Elliott et al. (2010) suggested 4 mm/yr of dextral motion along the Boundary fault, but there are no direct GPS measurements from this area. The more outboard Yakutat fault is assumed to have a northeast dip, shallower than the dip on the Boundary fault, and during the 1899 earthquake, the Yakutat fault experienced up to 3 m of coseismic uplift along the shoreline of northern Yakutat Bay. Our thermochronology data show that rocks of the Russell Fiord block have been exhumed from a depth of 2–3 km at very fast rates since ca. 1 Ma. The Boundary and the Yakutat faults were probably initiated by the mid- to late Miocene ca. 17–7 Ma and 13–6 Ma, respectively, resulting in moderate rates of exhumation (0.4–1 km/m.y.).

The rocks of the Russell Fiord block were juxtaposed with the Boundary block rocks, but their thermal histories appear to have developed independently. Their more recent history may be related to reverse faulting along the Boundary and Yakutat faults, as well as the intervening Calahonda fault. The independent thermal history of each block is supported by the fact that reverse faulting along the Boundary block exhumed rocks from depths with temperatures well above the ZFT closure window (>300 °C). However, the partially reset ZFT age distribution from rocks composing the hanging wall of the Yakutat fault indicates that they have been exhumed from much shallower depths, a pattern similar to rocks in the area around the Hubbard and Malaspina Glaciers (Enkelmann et al., 2015b).

An important question is how the Russell Fiord and Boundary blocks—and their bounding faults—relate to adjacent blocks farther into the orogenic corner to the north and northwest. West of Disenchantment Bay, the Boundary and the Yakutat faults seem to continue with a WNW strike into the Chaix Hills and the Esker Creek faults, respectively (Fig. 7). West of the Seward-Malaspina Glacier, the Chaix Hills fault continues with a WSW strike, juxtaposing older Cenozoic cover strata of the Yakutat microplate (Kultieth Formation) over Pliocene–Pleistocene glacial deposits of the Yakataga Formation (Chapman et al., 2012). Similarly, the Esker Creek fault is suggested to continue west of the syntaxis with a WSW trend as the Malaspina fault (Fig. 7B). Based on structural analyses (Chapman et al., 2012), ice-flow geomorphology (Cotton et al., 2014), and GPS modeling (Elliott et al., 2013), it is suggested that a shallow thrust is located underneath the western portion of the Malaspina Glacier, which represents the deformation front of the fold-and thrust belt (Fig. 7B). Mapping

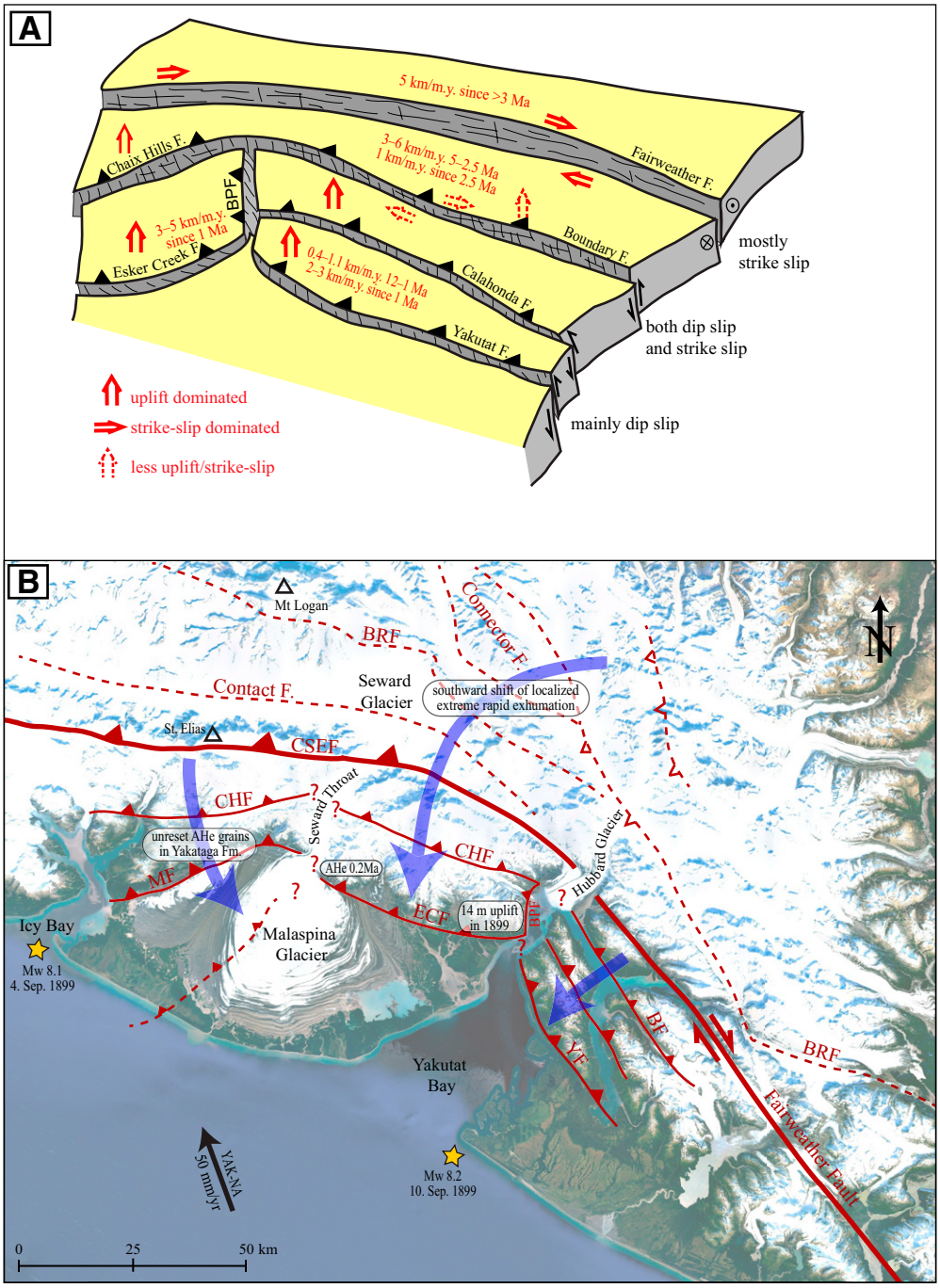

Figure 7. (A) Sketched model of the relative motion of fault-bounded blocks at the northern end of the Fairweather transform boundary (not to scale). BPF—Bancas Point fault. (B) Google Earth™ image of the St. Elias tectonic corner displaying topographic and glacial features, main known (solid) and inferred (dashed) structures, and location of the two 1899 earthquakes (yellow stars). Blue arrows show the spatial trend of deformation and exhumation. F.—fault, BRF—Border Ranges fault, CSEF—Chugach–St. Elias fault, CHF—Chaix Hills fault, ECF—Esker Creek fault, MF—Malaspina fault, BF—Boundary fault, YF—Yakutat fault, YAK-NA—Yakutat–North American plate. Plate motion is from Elliott et al. (2010).

within the fold-and-thrust belt suggests a southeastward propagation of thrusting (Chapman et al., 2012).

It remains unclear how the Chaix Hills and the Esker Creek faults connect with their western counterparts (Chaix Hills and Malaspina fault) and other structures in the fold-and thrust belt. The steep topography and rapidly moving ice in the Seward Throat prevent field observations of the structural bend. It is reasonable to assume that the complex intersections or transitions of these structures east and west of the Seward Throat resulted in breaking and weakening of rocks that allowed the development of the Seward Throat as a southern outlet of the Seward ice field (Fig. 7B). A similar observation can be made for Hubbard Glacier and Disenchantment Bay, which are located at the structural bend (Fig. 7B).

The finding of reverse-slip motion along faults parallel to the Fairweather transform plate boundary is in agreement with seismic studies that reveal partitioning of strain across the plate boundary onshore and offshore of the Yakutat microplate (Fig. 1; Doser and Lomas, 2000). Slip vectors along the southeastern margin of Alaska are parallel and up to 20° clockwise of the plate motion. West of the St. Elias syntaxis (Seward-Malaspina Glacier), the orientation of slip vectors changes to within 20° counterclockwise of the plate motion in the area of the Pamplona zone and the fold-and-thrust belt (Doser and Lomas, 2000; Elliott et al., 2013). The trend of the Boundary, Yakutat, and the Calahonda faults with respect to the plate motion favors strike-slip motion, whereas the trends of the Chaix Hills and the Esker Creek faults are more favorable for dip-slip motion and folding. This counterclockwise change in structural trend is documented in the exhumation pattern (Enkelmann et al., 2015a; this study) and the coseismic uplift pattern of the 1899 earthquake (Plafker and Thatcher, 2008), which indicate higher rates northwest of Disenchantment Bay (Figs. 5B and 7). Thus, taken together from the SE to the NW across the Yakutat tectonic corner, the structural trend bends ~90° counterclockwise from a NNW to a WSW trend, with a change from steeply dipping strike-slip–dominated to reverse- and thrust-dominated faults. Along the entire margin, there appears to be a southward propagation of deformation and exhumation within the Yakutat microplate and its Cenozoic cover strata (blue arrows in Fig. 7B).

Role of Climate

It is probable that erosional exhumation profoundly affected the uplifted hanging-wall rocks in this transpressional setting, and erosion was probably strongly influenced by glaciers. The efficiency of glacial erosion of the uplifted blocks may explain the fact that the exhumation occurred at such high rates of >3 km/m.y., especially in the last few million years. Erosion in the St. Elias Mountains is primarily accomplished by glaciers and specifically by tidewater glaciers in the Russell and Nunatak Fiord areas, which efficiently erode and transport sediment into the Gulf of Alaska (Gulick et al., 2015). Alpine glaciation of the St. Elias Mountains started by ca. 6–5 Ma and has intensified since the Pliocene-Pleistocene transition, when the global climate shifted to colder temperatures ca. 2.7 Ma (see Lagoe et al., 1993; Lisiecki and Raymo, 2005). This global climate shift resulted in the formation of large ice streams that crossed the Yakutat shelf and the formation of the Surveyor channel, which transported the majority of Holocene sediment into the distal deep-sea and Aleutian Trench (Manley and Kaufman, 2002; Gulick et al., 2015). The cyclicity of glaciation changed at the mid-Pleistocene transition ca. 1 Ma (Clark et al., 2006), and this change is believed to have resulted in a more erosive environment in the St. Elias Mountains (Berger et al., 2008b). However, clear evidence for such an influence of climate on the tectonic evolution of structures is missing on land (Enkelmann et al., 2010, 2015b, 2017), and it is missing in the offshore thermochronology record (Dunn et al., 2017).

We infer that Pliocene exhumation rates were very high for the Boundary block (Fig. 4C) and for rocks to the east along the Fairweather fault zone (Fig. 6). Increased exhumation rates are evident for the Russell Fiord block and the Bancas–Esker Creek block based on *t-T* path models (Fig. 4B) and the large detrital AFT age components (Figs. 6A). However, we did not find clear evidence that exhumation rates shifted at the Pliocene-Pleistocene transition, but we did find evidence for a shift to higher exhumation rates since ca. 4 Ma. Therefore, we suggest that these variations across the different blocks indicate that structure drives uplift and exhumation, rather than climate. The postulated shift at ca. 1 Ma to very rapid exhumation at the mid-Pleistocene transition may be reflected in the Russell Fiord block, but this is not recorded in the Boundary block. Instead, our data reveal a decrease in exhumation rates in the Boundary block since the intensification of glaciation starting at the Pliocene-Pleistocene transition. We therefore rule out the possibility that climate shifts have fundamentally influenced the exhumation pattern between the fault-bounded blocks, but we stress the importance of climate-driven surface processes for rock exhumation to occur at high rates in a convergent tectonic setting. This pattern is best displayed by the extremely rapid rates of rock exhumation over the last 1 m.y. along the Fairweather fault zone.

CONCLUSIONS

Thermochronologic data reveal the uplift and exhumation histories of the fault-bounded blocks along the northern end of the Fairweather fault, which separates the northwestward-moving Yakutat microplate from the North American plate. We found that the CMC rocks northeast of the Fairweather fault and those rocks in the fault zone were brought up from 10–12 km at extremely high rates (>5 km/m.y.) since ca. 3 Ma, which requires a significant component of dip-slip motion along the Fairweather fault. Adjacent rocks of the Boundary block appear to be allied with the Chugach–Prince William terrane rocks, and they were exhumed with similar rates and depths during the early Pliocene, perhaps when they were located ~250 km farther south and near the Baranof schist. Exhumation rates decreased (1 km/m.y.) since ca. 2 Ma, when the Boundary block moved along the Fairweather fault into the footwall position.

Upper Cretaceous to Paleocene flysch of the Russell Fiord block, between the Yakutat fault and the Boundary fault, experienced a thermal event at 50 Ma and then a relatively long period of burial until the late Miocene, when they were exhumed from 6–8 km depths. Exhumation was accommodated by reverse faulting along the Yakutat fault and the newly proposed Calahonda fault, which is parallel to the Yakutat fault (Fig. 7). Since 1 Ma, exhumation rates in the Russell Fiord block have been high (2 km/m.y.) and reveal an increase from the NW to the SE along its strike. This pattern of cooling may reflect tilting of the Russell Fiord block as it is thrust underneath the block located to the northwest, accommodated along the Bancas Point and Esker Creek faults (Fig. 7). This pattern of Pleistocene uplift and exhumation is in good agreement with the observed coseismic uplift of the shorelines along Russell Fiord, Yakutat Bay, and Disenchantment Bay (Plafker and Thatcher, 2008).

ACKNOWLEDGMENTS

This work was funded by the National Science Foundation grants EAR-1116554 and EAR-1728013 (Garver) and EAR-1116536 and EAR-1727991 (Davidson), and the American Chemical Society Petroleum Research Fund New Directions grant PRF-ND 54917 (Enkelmann). Undergraduate Research Grants from the American Association of Petroleum Geologists (AAPG) Foundation and the Department of Geology at the University of Cincinnati were awarded to A. Schartman. We appreciate access and permits from the U.S. National Forest to collect in the Tongass National Forest. We thank two anonymous reviewers, whose comments helped to improve the manuscript.

REFERENCES CITED

Abers, G.A., 2008, Orogenesis from subducting thick crust and evidence from Alaska, *in* Freymuller, J.T., Haeussler, P.J., Wesson, R.L., and Ekström, G., eds., Active Tectonics and Seismic Potential of Alaska: American Geophysical Union Geophysical Monograph 179, p. 337–349, https://doi.org/10.1029/179GM19.

Arnston, E., Davidson, C.M., and Garver, J.I., 2017, Geochemistry, U/Pb ages, and Hf isotopes of the Mt. Draper and Mt. Stamy Plutons, Nunatak Fjord, Alaska: Implications for the Sanak-Baranof plutonic belt: Geological Society of America Annual Meeting Abstracts with Programs, v. 49, no. 4, paper 28-6.

Berger, A.L., Spotila, J.A., Chapman, J.B., Pavlis, T.L., Enkelmann, E., Ruppert, N.A., and Buscher, J.T., 2008a, Architecture, kinematics, and exhumation of a convergent orogenic wedge: A thermochronological investigation of tectonic-climatic interactions within the central St. Elias orogen, Alaska: Earth and Planetary Science Letters, v. 270, p. 13–24, https://doi.org/10.1016/j.epsl.2008.02.034.

Berger, A.L., Gulick, S.P.S., Spotila, J.A., Upton, P., Jaeger, J.M., Chapman, J.B., Worthington, L.A., Pavlis, T.L., Ridgway, K.D., Willems, B.A., and McAleer, R.J., 2008b, Quaternary tectonic response to intensified glacial erosion in an orogenic wedge: Nature Geoscience, v. 1, no. 11, p. 793–799, https://doi.org/10.1038/ngeo334.

Brandon, M.T., 1996, Probability density plot for fission-track grain-age samples: Radiation Measurements, v. 26, no. 5, p. 663–676, https://doi.org/10.1016/S1350-4487(97)82880-6.

Brandon, M.T., Roden-Tice, M.K., and Garver, J.I., 1998, Late Cenozoic exhumation of the Cascadia accretionary wedge in the Olympic Mountains, northwest Washington State: Geological Society of America Bulletin, v. 110, no. 8, p. 985–1009, https://doi.org/10.1130/0016-7606(1998)110<0985:LCEOTC>2.3.CO;2.

Bruhn, R.L., Pavlis, T.L., Plafker, G., and Serpa, L., 2004, Deformation during terrane accretion in the Saint Elias orogen, Alaska: Geological Society of America Bulletin, v. 116, p. 771–787, https://doi.org/10.1130/B25182.1.

Bruhn, R.L., Sauber, J., Cotton, M.M., Pavlis, T.L., Burgess, E., Ruppert, N., and Forster, R.R., 2012, Plate margin deformation and active tectonics along the northern edge of the Yakutat terrane in the Saint Elias orogen, Alaska, and Yukon, Canada: Geosphere, v. 8, p. 1384–1407, https://doi.org/10.1130/GES00807.1.

Bruns, T.R., 1983, Model for the origin of the Yakutat block, an accreted terrane in the northern Gulf of Alaska: Geology, v. 11, no. 12, p. 718–721, https://doi.org/10.1130/0091-7613(1983)11<718:MFTOOT>2.0.CO;2.

Chapman, J.B., Pavlis, T.L., Bruhn, R.L., Worthington, L.L., Gulick, S.P., and Berger, A.L., 2012, Structural relationships in the eastern syntaxis of the St. Elias orogen, Alaska: Geosphere, v. 8, p. 105–126, https://doi.org/10.1130/GES00677.1.

Christeson, G.L., Gulick, S.P., Van Avendonk, H.J., Worthington, L.L., Reece, R.S., and Pavlis, T.L., 2010, The Yakutat terrane: Dramatic change in crustal thickness across the Transition fault, Alaska: Geology, v. 38, p. 895–898, https://doi.org/10.1130/G31170.1.

Clark, P.U., Archer, D., Pollard, D., Blum, J.D., Rial, J.A., Brovkin, V., Mix, A.C., Pisias, N.G., and Roy, M., 2006, The middle Pleistocene transition: Characteristics, mechanisms, and implications for long-term changes in atmospheric pCO_2: Quaternary Science Reviews, v. 25, no. 23, p. 3150–3184, https://doi.org/10.1016/j.quascirev.2006.07.008.

Cotton, M.M., Bruhn, R.L., Sauber, J., Burgess, E., and Forster, R.R., 2014, Ice surface morphology and flow on Malaspina Glacier, Alaska: Implications for regional tectonics in the Saint Elias orogen: Tectonics, v. 33, p. 581–595, https://doi.org/10.1002/2013TC003381.

Cui, Y., Miller, D., Schiarizza, P., and Diakow, L.J., 2017, British Columbia Digital Geology: British Columbia Ministry of Energy, Mines and Petroleum Resources, British Columbia Geological Survey Open-File 2017–8, 9 p.

Davidson, C.M., and Garver, J.I., 2017, Age and origin of the Resurrection ophiolite and associated turbidites of the Chugach–Prince William terrane, Kenai Peninsula, Alaska: The Journal of Geology, v. 125, no. 6, p. 681–700, https://doi.org/10.1086/693926.

Dolcimascolo, A., Davidson, C., Garver, J., and Sophis, J., 2017, Provenance of and age of granitoid and sandstone clasts in conglomerates of the Paleocene to Upper Cretaceous Yakutat Group, Russell Fjord, Alaska: Geological Society of America Annual Meeting. Abstracts with Programs, v. 49, no. 4, paper 47-5.

Doser, D.I., 2012, Revisiting the 1979 St. Elias, Alaska, aftershock sequence and its regional significance: Bulletin of the Seismological Society of America, v. 102, p. 2392–2404, https://doi.org/10.1785/0120120007.

Doser, D.I., 2014, Seismicity of southwestern Yukon, Canada, and its relation to slip transfer between the Fairweather and Denali fault systems: Tectonophysics, v. 611, p. 121–129, https://doi.org/10.1016/j.tecto.2013.11.018.

Doser, D.I., and Lomas, R., 2000, The transition from strike-slip to oblique subduction in southeastern Alaska from seismological studies: Tectonophysics, v. 316, p. 45–65, https://doi.org/10.1016/S0040-1951(99)00254-1.

Dunn, C.A., Enkelmann, E., Ridgway, K.D., and Allen, W.K., 2017, Source to sink evaluation of sediment routing in the Gulf of Alaska and southeast Alaska: A thermochronometric perspective: Journal of Geophysical Research–Earth Surface, v. 122, no. 3, p. 711–734, https://doi.org/10.1002/2016JF004168.

Dusel-Bacon, C., Csejtey, B., Foster, H.L., Doyle, E.O., Nokleberg, W.J., and Plafker, G., 1993, Distribution, Facies, Ages, and Proposed Tectonic Associations of Regionally Metamorphosed Rocks in East- and South-Central Alaska: U.S. Geological Society Professional Paper 1497-C, 73 p.

Ehlers, T.A., and Farley, K.A., 2003, Apatite (U-Th)/He thermochronometry: Methods and applications to problems in tectonic and surface processes: Earth and Planetary Science Letters, v. 206, p. 1–14, https://doi.org/10.1016/S0012-821X(02)01069-5.

Ehlers, T.A., Szameitat, A., Enkelmann, E., Yanites, B.J., and Woodsworth, G.J., 2015, Identifying spatial variations in glacial erosion with detrital thermochronology, Coast Mountains British Columbia: Journal of Geophysical Research–Earth Surface, v. 120, p. 1023–1039, https://doi.org/10.1002/2014JF003432.

Elliott, J.L., Larsen, C.F., Freymueller, J.T., and Motyka, R.J., 2010, Tectonic block motion and glacial isostatic adjustment in southeast Alaska and adjacent Canada constrained by GPS measurements: Journal of Geophysical Research–Solid Earth, v. 115, B09407, https://doi.org/10.1029/2009JB007139.

Elliott, J.L., Freymueller, J.T., and Larsen, C.F., 2013, Active tectonics of the St. Elias orogen, Alaska, observed with GPS measurements: Journal of Geophysical Research–Solid Earth, v. 118, p. 5625–5642, https://doi.org/10.1002/jgrb.50341.

Enkelmann, E., Garver, J.I., and Pavlis, T.L., 2008, Rapid exhumation of ice-covered rocks of the Chugach–St. Elias orogen, SE-Alaska: Geology, v. 36, p. 915–918, https://doi.org/10.1130/G2252A.1.

Enkelmann, E., Zeitler, P.K., Garver, J.I., Pavlis, T.L., and Hooks, B.P., 2010, The thermochronological record of tectonic and surface process interaction at the Yakutat–North American collision zone in southeast Alaska: American Journal of Science, v. 310, p. 231–260, https://doi.org/10.2475/04.2010.01.

Enkelmann, E., Valla, P.G., and Champagnac, J.-D., 2015a, Low temperature thermochronology of the Yakutat plate corner, St. Elias Range (Alaska): Bridging short-term and long-term deformation: Quaternary Science Reviews, v. 113, p. 23–38, https://doi.org/10.1016/j.quascirev.2014.10.019.

Enkelmann, E., Koons, P.O., Pavlis, T.L., Hallet, B., Barker, A., Elliott, J., Garver, J.I., Gulick, S.P.S., Headley, R.M., Pavlis, G.L., Ridgway, K.D., Ruppert, N., and Van Avendonk, H.J.A., 2015b, Cooperation among tectonic and surface processes in the St. Elias Range, Earth's highest coastal mountains: Geophysical Research Letters, v. 42, p. 5838–5846, https://doi.org/10.1002/2015GL064727.

Enkelmann, E., Piestrzeniewicz, A., Falkowski, S., Stübner, K., and Ehlers, T.A., 2017, Thermochronology in southeast Alaska and southwest Yukon: Implications for North American plate response to terrane accretion: Earth and Planetary Science Letters, v. 457, p. 348–358, https://doi.org/10.1016/j.epsl.2016.10.032.

Falkowski, S., and Enkelmann, E., 2016, Upper crustal cooling of the Wrangellia Composite Terrane in the northern St. Elias Mountains, western Canada: Lithosphere, v. 8, p. 359–378, https://doi.org/10.1130/L508.1

Falkowski, S., Enkelmann, E., and Ehlers, T.A., 2014, Constraining the area of rapid and deep-seated exhumation at the Yakutat plate corner, southeast Alaska: Tectonics, v. 33, p. 597–616, https://doi.org/10.1002/2013TC003408.

Falkowski, S., Enkelmann, E., Drost, K., Pfänder, J.A., Stübner, K., and Ehlers, T.A., 2016, Cooling history of the St. Elias syntaxis, southeast Alaska, revealed by geo- and thermochronology of cobble-size glacial detritus: Tectonics, v. 35, p. 447–468, https://doi.org/10.1002/2015TC004086.

Farley, K.A., 2002, (U-Th)/He dating: Techniques, calibrations, and applications: Reviews in Mineralogy and Geochemistry, v. 47, p. 819–844, https://doi.org/10.2138/rmg.2002.47.18.

Farris, D.W., and Paterson, S.R., 2009, Subduction of a segmented ridge along a curved continental margin: Variations between the western and eastern Sanak-Baranof belt, southern Alaska: Tectonophysics, v. 464, p. 100–117, https://doi.org/10.1016/j.tecto.2007.10.008.

Finzel, E.S., Trop, J.M., Ridgway, K.D., and Enkelmann, E., 2011, Upper plate proxies for flat-slab subduction processes in southern Alaska: Earth and Planetary Science Letters, v. 303, p. 348–360, https://doi.org/10.1016/j.epsl.2011.01.014.

Fitzgerald, P.G., Baldwin, S.I., Webb, L.E., and O'Sullivan, P.B., 2006, Interpretation of (U-Th)/He single grain ages from slowly cooled crustal terranes: A case study from the Transantarctic Mountains of southern Victoria Land: Chemical Geology, v. 225, p. 91–120, https://doi.org/10.1016/j.chemgeo.2005.09.001.

Fletcher, H.J., and Freymueller, J.T., 1999, New GPS constraints on the motion of the Yakutat block: Geophysical Research Letters, v. 26, p. 3029–3032, https://doi.org/10.1029/1999GL005346.

Flowers, R.M., Shuster, D.L., Wernicke, B.P., and Farley, K.A., 2007, Radiation damage control on apatite (U-Th)/He dates from the Grand Canyon region, Colorado Plateau: Geology, v. 35, no. 5, p. 447, https://doi.org/10.1130/G23471A.1.

Flowers, R.M., Ketcham, R.A., Shuster, D.L., and Farley, K.A., 2009, Apatite (U-Th)/He thermochronometry using a radiation damage accumulation and annealing model: Geochimica et Cosmochimica Acta, v. 73, no. 8, p. 2347–2365, https://doi.org/10.1016/j.gca.2009.01.015.

Ford, A.L.J., Forster, R.R., and Bruhn, R.L., 2003, Ice surface velocity patterns on Seward Glacier, Alaska-Yukon, and their implications for regional tectonics in the Saint Elias Mountains: Annals of Glaciology, v. 36, p. 21–28, https://doi.org/10.3189/172756403781816086.

Gardner, M.C., Bergman, S.C., Cushing, G.W., MacKevett, E.M., Plafker, G., Campbell, R.B., Dodds, C.J., McClelland, W.C., and Mueller, P.A., 1988, Pennsylvanian pluton stitching of Wrangellia and the Alexander terrane, Wrangell Mountains, Alaska: Geology, v. 16, p. 967–971, https://doi.org/10.1130/0091-7613(1988)016<0967:PPSOWA>2.3.CO;2.

Garver, J.I., and Davidson, C.M., 2015, Southwestern Laurentian zircons in Upper Cretaceous flysch of the Chugach–Prince William terrane in Alaska: American Journal of Science, v. 315, p. 537–556, https://doi.org/10.2475/06.2015.02.

Garver, J.I., and Davidson, C.M., 2017, Accretion and translation of the Chugach, Prince William, and Yakutat terranes in Alaska: Geological Society of America Annual Meeting Abstracts with Programs, v. 49, no. 6, paper 223-7, https://doi.org/10.1130/abs/2017AM-302956

Garver, J.I., and Kamp, P.J.J., 2002, Integration of zircon color and zircon fission track zonation patterns in orogenic belts: Application of the Southern Alps, New Zealand: Tectonophysics, v. 349, p. 203–219, https://doi.org/10.1016/S0040-1951(02)00054-9.

Gasser, D., Bruand, E., Stüwe, K., Foster, D.A., Schuster, R., Fügenschuh, B., and Pavlis, T.L., 2011, Formation of a metamorphic complex along an obliquely convergent margin: Structural and thermochronological evolution of the Chugach metamorphic complex, southern Alaska: Tectonics, v. 30, TC2012, https://doi.org/10.1029/2010TC002776.

Green, P.F., Duddy, I.R., Gleadow, A.J.W., Tingate, P.T., and Laslett, G.M., 1986, Thermal annealing of fission tracks in apatite: 1. A qualitative description: Chemical Geology–Isotopic Geoscience Section, v. 59, no. 4, p. 237–253, https://doi.org/10.1016/0009-2541(86)90048-3.

Guenthner, W.R., Reiners, P.W., Ketcham, R.A., Nasdala, L., and Giester, G., 2013, Helium diffusion in natural zircon: Radiation damage, anisotropy, and the interpretation of zircon (U-TH)/He thermochronology: American Journal of Science, v. 313, p. 145–198, https://doi.org/10.2475/03.2013.01.

Guenthner, W.R., Reiners, P.W., and Tian, Y., 2014, Interpreting date-eU correlations in zircon (U-Th)/He datasets: A case study from the Longmen Shan, China: Earth and Planetary Science Letters, v. 403, p. 328–339, https://doi.org/10.1016/j.epsl.2014.06.050.

Gulick, S.P., Lowe, L.A., Pavlis, T.L., Gardner, J.V., and Mayer, L.A., 2007, Geophysical insights into the transition fault debate: Propagating strike-slip in response to stalling Yakutat

block subduction in the Gulf of Alaska: Geology, v. 35, p. 763–766, https://doi.org/10.1130/G23585A.1.

Gulick, S.P.S., Jaeger, J.M., Mix, A.C., Asahi, H., Bahlburg, H., Belanger, C., Berbel, C.B.B., Childress, L., Cowan, E., Drab, L., Forwick, M., Fukumura, A., Ge, S., Gupta, S., Kioka, A., Konno, S., LeVay, L., März, C., Matsuzaki, K., McClymont, E., Moy, C., Müller, J., Nakamura, A., Ojima, T., Ribeiro, F.R., Ridgway, K., Romero, O., Slagle, A., Stoner, J., St-Onge, G., Suto, I., Walczak, M.D., Worthington, L., Bailey, I., Enkelmann, E., Reece, R., and Schwarz, J.M., 2015, Mid-Pleistocene climate transition drives net mass loss from rapidly uplifting St. Elias Mountains, Alaska: Proceedings of the National Academy of Sciences of the United States of America, v. 112, no. 49, p. 15,042–15,047, https://doi.org/10.1073/pnas.1512549112.

Haeussler, P.J., 2008, An overview of the neotectonics of interior Alaska: Far-field deformation from the Yakutat microplate collision, *in* Freymuller, J.T., Haeussler, P.J., Wesson, R.L., and Ekström, G., eds., Active Tectonics and Seismic Potential of Alaska: American Geophysical Union Geophysical Monograph 179, p. 83–108, https://doi.org/10.1029/179GM05.

Haeussler, P.J., Bradley, D.C., Goldfarb, R.J., Snee, L.W., and Taylor, C.D., 1995, Link between ridge subduction and gold mineralization in southern Alaska: Geology, v. 23, no. 11, p. 995–998, https://doi.org/10.1130/0091-7613(1995)023<0995:LBRSAG>2.3.CO;2.

Haeussler, P.J., Bradley, D.C., Wells, R.E., and Miller, M.L., 2003, Life and death of the Resurrection plate: Evidence for its existence and subduction in the northeastern Pacific in Paleocene–Eocene time: Geological Society of America Bulletin, v. 115, no. 7, p. 867–880, https://doi.org/10.1130/0016-7606(2003)115<0867:LADOTR>2.0.CO;2.

Hudson, T., Plafker, G., and Turner, D.L., 1977, Metamorphic rocks of the Yakutat–St. Elias area, south-central Alaska: Journal of Research of the U.S. Geological Survey, v. 5, p. 173–184.

Hudson, T., Plafker, G., and Petermanm, Z.E., 1979, Paleogene anatexis along the Gulf of Alaska margin: Geology, v. 7, p. 573–577, https://doi.org/10.1130/0091-7613(1979)7<573:PAATGO>2.0.CO;2.

Jones, D.L., Silberling, N.J., and Hillhouse, J., 1977, Wrangellia: A displaced terrane in northwestern North America: Canadian Journal of Earth Sciences, v. 14, p. 2565–2577, https://doi.org/10.1139/e77-222.

Ketcham, R.A., 2005, Forward and inverse modeling of low-temperature thermochronometry data: Reviews in Mineralogy and Geochemistry, v. 58, p. 275–314, https://doi.org/10.2138/rmg.2005.58.11.

Lagoe, M.B., Eyles, C.H., Eyles, N., and Hale, C., 1993, Timing of late Cenozoic tidewater glaciation in the far North Pacific: Geological Society of America Bulletin, v. 105, no. 12, p. 1542–1560, https://doi.org/10.1130/0016-7606(1993)105<1542:TOLCTG>2.3.CO;2.

Lisiecki, L.E., and Raymo, M.E., 2005, A Pliocene–Pleistocene stack of 57 globally distributed benthic $\delta^{18}O$ records: Paleoceanography, v. 20, PA1003, https://doi.org/10.1029/2004PA001071.

Little, T.A., Cox, S., Vry, J.K., and Batt, G., 2005, Variations in exhumation level and uplift rate along the oblique-slip Alpine fault, central Southern Alps, New Zealand: Geological Society of America Bulletin, v. 117, p. 707–723, https://doi.org/10.1130/B25500.1.

Lock, J., and Willett, S., 2008, Low-temperature thermochronometric ages in fold-and-thrust belts: Tectonophysics, v. 456, p. 147–162, https://doi.org/10.1016/j.tecto.2008.03.007.

Manley, W.F., and Kaufman, D.S., 2002, Alaska PaleoGlacier Atlas: Boulder, Colorado, Institute of Arctic and Alpine Research (INSTAAR), University of Colorado, http://instaar.colorado.edu/QGISL/ak_paleoglacier_atlas (accessed 2017).

McAleer, R.J., Spotila, J.A., Enkelmann, E., and Berger, A.L., 2009, Exhumation along the Fairweather fault, southeastern Alaska, based on low-temperature thermochronometry: Tectonics, v. 28, TC1007, https://doi.org/10.1029/2007TC002240.

Miller, D.J., 1961, Geology of the Southeastern Part of the Robinson Mountains Yakataga District, Alaska: U.S. Geological Survey Oil and Gas Investigation Map OM-187, scale 1:63,360.

Olson, H., Sophis, J., Davidson, C., and Garver, J., 2017, Detrital zircon from the Yakutat terrane: Differentiating the Yakutat Group and the schist of Nunatak Fjord: Geological Society of America Annual Meeting Abstracts with Programs, v. 49, no. 4, paper 29-6, https://doi.org/10.1130/abs/2017CD-292889.

Pavlis, T.L., Picornell, C., and Serpa, L., 2004, Tectonic processes during oblique collision: Insights from the St. Elias orogen, northern North American Cordillera: Tectonics, v. 23, TC3001, https://doi.org/10.1029/2003TC001557.

Perry, S.E., Garver, J.I., and Ridgway, K.D., 2009, Transport of the Yakutat terrane, southern Alaska: Evidence from sediment petrology and detrital zircon fission-track and U/Pb double dating: The Journal of Geology, v. 117, p. 156–173, https://doi.org/10.1086/596302.

Plafker, G., 1987, Regional geology and petroleum potential of the northern Gulf of Alaska continental margin, *in* Scholl, D.W., et al., eds., Geology and Resource Potential of the Continental Margin of Western North America and Adjacent Ocean Basins—Beaufort Sea to Baja California: Houston, Texas, Circum-Pacific Council for Energy and Mineral Resources, Earth Science Series 6, p. 229–268.

Plafker, G., and Thatcher, W., 2008, Geological and geophysical evaluation of the mechanisms of the great 1899 Yakutat Bay earthquakes, *in* Freymueller J.T., et al., eds., Active Tectonics and Seismic Potential of Alaska: American Geophysical Union Geophysical Monograph 179, p. 215–236, https://doi.org/10.1029/179GM12.

Plafker, G., Nokleberg, W.J., and Lull, J.S., 1989, Bedrock geology and tectonic evolution of the Wrangellia, Peninsular, and Chugach terranes along the Trans-Alaskan Crustal Transect in the northern Chugach Mountains and southern Copper River basin, Alaska: Journal of Geophysical Research, v. 94, p. 4255–4295, https://doi.org/10.1029/JB094iB04p04255.

Plafker, G., Moore, J.C., and Winkler, G.R., 1994, Geology of the southern Alaska margin, *in* Plafker, G., and Berg, H.G., eds., The Geology of Alaska: Boulder, Colorado, Geological Society of America, Geology of North America, v. G-1, p. 389–450.

Rahn, M.K., Brandon, M.T., Batt, G.E., and Garver, J.I., 2004, A zero-damage model for fission-track annealing in zircon: The American Mineralogist, v. 89, p. 473–484, https://doi.org/10.2138/am-2004-0401.

Raup, B.H., Racoviteanu, A., Khalsa, S.J.S., Helm, C., Armstrong, R., and Arnaud, Y., 2007, The GLIMS Geospatial Glacier Database: A new tool for studying glacier change: Global and Planetary Change, v. 56, p. 101–110, https://doi.org/10.1016/j.gloplacha.2006.07.018.

Reiners, P.W., 2005, Zircon (U-Th)/He thermochronometry, *in* Reiners, P.W., and Ehlers, T.A., eds., Low-Temperature Thermochronology: Technique, Interpretation, and Applications: Reviews in Mineralogy and Geochemistry, v. 58, p. 151–176.

Reiners, P.W., and Brandon, M.T., 2006, Using thermochronology to understand orogenic erosion: Annual Review of Earth and Planetary Sciences, v. 34, p. 419–466, https://doi.org/10.1146/annurev.earth.34.031405.125202.

Richter, D.H., Smith, J.G., Lanphere, M.A., Dalrymple, G.B., Reed, B.L., and Shew, N., 1990, Age and progression of volcanism, Wrangell volcanic field, Alaska: Bulletin of Volcanology, v. 53, p. 29–44, https://doi.org/10.1007/BF00680318.

Richter, D.H., Preller, C.C., Labay, K.A., and Shew, N.B., 2006, Geologic Map of the Wrangell–Saint Elias National Park and Preserve, Alaska: U.S. Geological Survey Scientific Investigations Map 2877 (and explanation), scale 1:350,000.

Sauber, J., McClusky, S., and King, R., 1997, Relation of ongoing deformation rates to subduction zone processes in southern Alaska: Geophysical Research Letters, v. 24, p. 2853–2856, https://doi.org/10.1029/97GL52979.

Sisson, V.B., Poole, A.R., Harris, N.R., Cooper Burner, H., Pavlis, T.L., Copeland, P., Donelick, R.A., and McClelland, W.C., 2003, Geochemical and geochronologic constraints for genesis of a tonalite-trondhjemite suite and associated mafic intrusive rocks in the eastern Chugach Mountains, Alaska: A record of ridge-transform subduction, *in* Sisson, V.B., Roeske, S.M., and Pavlis, T.L., eds., Geology of a Transpressional Orogen Developed during Ridge-Trench Interaction along the North Pacific Margin: Geological Society of America Special Paper 371, p. 293–326, https://doi.org/10.1130/0-8137-2371-X.293.

Sophis, J.M., Garver, J.I., Davidson, C.M., Dolcimascolo, A., and Olson, H., 2017, Provenance and age distribution of detrital zircon in the Upper Cretaceous–Paleocene flysch and mélange of the Yakutat Group, Yakutat Bay and Russell Fjord, Alaska: Geological Society of America Annual Meeting Abstracts with Programs, v. 49, no. 4, paper 29-7, https://doi.org/10.1130/abs/2017CD-292959.

Spotila, J.A., Farley, K.A., and Sieh, K., 1998, Uplift and erosion of the San Bernardino Mountains associated with transpression along the San Andreas fault, California, as constrained by radiogenic helium thermochronology: Tectonics, v. 17, p. 360–378, https://doi.org/10.1029/98TC00378.

Stock, G.M., Ehlers, T.A., and Farley, K.A., 2006, Where does sediment come from? Quantifying catchment erosion with detrital apatite (U-Th)/He thermochronometry: Geology, v. 34, p. 725–728, https://doi.org/10.1130/G22592.1.

Suarez, K.A., 2016, Thermal evolution and provenance revealed through detrital zircon fission track dating of the Yakutat Group, Yakutat Bay, Alaska [BSc Thesis]: Schenectady, New York, Union College, 60 p.

Tarr, R.S., and Butler, B.S., 1909, The Yakutat Bay Region, Alaska: U.S. Geological Survey Professional Paper 64, 183 p.

Tarr, R.S., and Martin, L., 1912, The Earthquakes at Yakutat Bay, Alaska, with a Preface by G. K. Gilbert: U.S. Geological Survey Professional Paper 69, 135 p.

Tocher, D., 1960, The Alaska earthquake of July 10, 1958: Movement on the Fairweather fault and field investigation of southern epicentral region: Bulletin of the Seismological Society of America, v. 50, no. 2, p. 267–292.

Trop, J.M., and Ridgway, K.D., 2007, Mesozoic and Cenozoic tectonic growth of southern Alaska: A sedimentary basin perspective, *in* Ridgway, K.D., Trop, J.M., Glen, J.M.G., and O'Neill, J.M., eds., Tectonic Growth of a Collisional Continental Margin: Crustal Evolution of Southern Alaska: Geological Society of America Special Paper 431, p. 55–94, https://doi.org/10.1130/2007.2431(04).

Trop, J.M., Ridgway, K.D., Manuszak, J.D., and Layer, P.W., 2002, Sedimentary basin development on the allochthonous Wrangellia composite terrane, Mesozoic Wrangell Mountains basin, Alaska: A long-term record of terrane migration and arc construction: Geological Society of America Bulletin, v. 114, p. 693–717, https://doi.org/10.1130/0016-7606(2002)114,0693:MSBDOT. 2.0.CO;2.

Wilson, F.H., Hults, C.P., Mull, C.G., and Karl, S.M., comps., 2015, Geologic Map of Alaska: U.S. Geological Survey Scientific Investigations Map 3340, pamphlet 196 p., 2 sheets, scale 1:1,584,000, https://doi.org/10.3133/sim3340.

Worthington, L.L., Van Avendonk, H.J., Gulick, S.P., Christeson, G.L., and Pavlis, T.L., 2012, Crustal structure of the Yakutat terrane and the evolution of subduction and collision in southern Alaska: Journal of Geophysical Research–Solid Earth, v. 117, no. B1, B01102, https://doi.org/10.1029/2011JB008493.

Zellers, S.D., 1995, Foraminiferal sequence biostratigraphy and seismic stratigraphy of a tectonically active margin; the Yakataga Formation, northeastern Gulf of Alaska: Marine Micropaleontology, v. 26, p. 255–271, https://doi.org/10.1016/0377-8398(95)00031-3.

MANUSCRIPT RECEIVED 30 MAY 2018
REVISED MANUSCRIPT RECEIVED 16 OCTOBER 2018
MANUSCRIPT ACCEPTED 5 DECEMBER 2018